2022 Radiology Research Symposium

Program and Abstracts

August 4, 2022

UC DAVIS HEALTH | Department of Radiology

2022 Radiology Research Symposium Program and Abstract Table of Contents

Chair's message

We are excited to welcome you to the 1st Annual Radiology Research Symposium. Our faculty have a wide array of research interests from basic imaging methodology and pre-clinical to molecular imaging clinical trials and biomedical imaging informatics.

Our department is a pioneer in innovation, applying the latest techniques, technology and diagnostic methodology to deliver integrated, evidence-based patient centered care. The development of the EXPLORER PET/CT program has demonstrated that our Physics Division is home to expert leaders in the field who are on the forefront of imaging and patient care. Our Nuclear Medicine Division is innovating in the realm of theranostics with novel methods to combine imaging and therapy for a "smart bomb" for cancer and related diseases. Our Clinical Divisions are involved in translational research in collaboration with numerous other departments and centers.

We are building an Artificial Intelligence Research Group as Radiology will be on the forefront of developing, integrating and adopting machine learning techniques into the patient care continuum. We have faculty interested in detection and risk algorithms as well as natural language processing algorithms. We believe that AI technology will rapidly change the way radiology as well as healthcare in general will be delivered.

Radiology touches virtually all patients in the healthcare system and we are always on the forefront of technological development. We are excited to share with you what we are doing currently and how we see the future of healthcare.

Thank-you for joining us and enjoy the program!

Elizabeth A. Morris, M.D.

Chair, Department of Radiology

2022 Radiology Research Symposium Program

3:00 pm Chair's Introduction - Elizabeth Morris, MD

3:05 pm VC Research Introduction - Ramsey Badawi, PhD

3:10 pm Session 1: Invited talks, 8 minutes each, 2 minutes questions

Looking aHead: Simultaneous PET/MRI for Brain at UC Davis	Audrey Fan, PhD
Diagnostic and Quality Improvement Insights Enabled by a Comprehensive NLP Pipeline for Radiology and Pathology Reports	Tom Loehfelm, MD
"3D PrintViz" Laboratory: UC Davis's Medical 3D Printing and Visualization Laboratory	Osama Raslan, MD
Industry Partnerships to develop Advanced PET Scanners	Simon Cherry, PhD
Engaging health disparities in biomedical imaging research	Felipe Godinez, PhD

4:00 pm Coffee Break

4:15 pm Session II: Proffered talks, 6 minutes each, 2 minutes questions

High resolution CT for lung nodule characterization: a multi-reader comparison against conventional normal resolution CT	Anthony Chen, MD
Molecular Imaging of Nonalcoholic Steatohepatitis (NASH): A Collaborative Team Effort at UC Davis Health	Guobao Wang, PhD
Automated whole brain segmentation of T_2w MRI brain scans of rats exposed to organophosphates using a U-Net neural network	Valerie Porter, BS
Effect on Intra-procedural Metrics of Pre-procedural CT Angiography prior to Conventional Angiography in Trauma Patients with Active Extravasation on Initial Portal Venous Phase Imaging	Frank Liou, MD
CD8-Targeted Total-Body PET Imaging of T Cells in Patients Recovering from COVID-19	Negar Omidvari, PhD
Meniscus MRI	Cyrus Bateni, MD
High-grade pediatric renal trauma: prognostic value of ureteral contrast	Philip Kim, MD
Total-body perfusion imaging using [^{11}C]-butanol	Elizabeth Li, PhD
AI-based Automated Lipomatous Tumor Segmentation in MR Images	Quinn Ng, MD, PhD
First-in-human imaging and dosimetry of novel integrin [^{18}F]αvβ6 binding peptide in patients with metastatic carcinoma	Cameron Foster, MD

5:35 pm Prizes: Best resident abstract, best graduate student abstract, best postdoctoral fellow abstract — Ramsey Badawi, PhD

5:40 pm Posters and Food

7:00 pm Close

Oral Abstracts

Looking aHead: Simultaneous PET/MRI for Brain at UC Davis	Audrey Fan
Diagnostic and Quality Improvement Insights Enabled by a Comprehensive NLP Pipeline for Radiology and Pathology Reports	Tom Loehfelm
“3D PrintViz” Laboratory: UC Davis’s Medical 3D Printing and Visualization Laboratory	Osama Raslan
Industry Partnerships to develop Advanced PET Scanners	Simon Cherry
Engaging health disparities in biomedical imaging research	Felipe Godinez
High resolution CT for lung nodule characterization: a multi-reader comparison against conventional normal resolution CT	Anthony Chen
Molecular Imaging of Nonalcoholic Steatohepatitis (NASH): A Collaborative Team Effort at UC Davis Health	Guobao Wang
Automated whole brain segmentation of T_2w MRI brain scans of rats exposed to organophosphates using a U-Net neural network	Valerie Porter
Effect on Intra-procedural Metrics of Pre-procedural CT Angiography prior to Conventional Angiography in Trauma Patients with Active Extravasation on Initial Portal Venous Phase Imaging	Frank Liou
CD8-Targeted Total-Body PET Imaging of T Cells in Patients Recovering from COVID-19	Negar Omidvari
Meniscus MRI	Cyrus Bateni
High-grade pediatric renal trauma: prognostic value of ureteral contrast	Philip Kim
Total-body perfusion imaging using [^{11}C]-butanol	Elizabeth Li
AI-based Automated Lipomatous Tumor Segmentation in MR Images	Quinn Ng
First-in-human imaging and dosimetry of novel integrin [^{18}F]αvβ6 binding peptide in patients with metastatic carcinoma	Cameron Foster

Looking aHead: Simultaneous PET/MRI for Brain at UC Davis

[1]Audrey P. Fan, [1,2]Ramsey D. Badawi, [2]Sun Il Kwon, [1,2]Simon R. Cherry, [3]James Schellenberg, [1]Felipe Godinez

[1]Department of Radiology, UC Davis, [2]Department of Biomedical Engineering, UC Davis, [3]Cubresa, Inc., Winnipeg, Canada

Introduction: Simultaneous acquisition of MRI and PET enables novel measurements of functional-metabolic dynamics in brain function; and mitigates patient burden and radiation dose in complex neurological disorders that require multiple scan modalities. The BrainPET (Cubresa, Inc.) is a PET insert for a whole-body 3T MRI scanner that provides PET/MRI imaging capacity for brain scans in a cost-efficient and accessible manner. The BrainPET design targets 5.4% sensitivity and 1.5-2.0 mm PET spatial resolution with silicon photomultiplier scintillators; and accommodates high MRI signal-to-noise ratio with 32 radiofrequency receive channels.

Planned Collaboration: UC Davis Health Departments of Radiology and Neurology have a memorandum of understanding with Cubresa to develop, test, and apply the BrainPET in new brain disease settings. Specific technical collaborations will include (a) development of time-of-flight capabilities (target 200-300ps); (b) rigorous assessment of quantitative accuracy for dynamic PET scans at different count rates; and (c) evaluation of MRI-based attenuation correction methods for the PET images. For neurological disease applications, our initial target patient population will recruit from the UC Davis Alzheimer's Disease Research Center, which studies a diverse elderly cohort with mixed neurodegenerative pathologies and early cognitive impairment. A subset of ADRC patients currently receive PET scans with new radioligands to assess amyloid ([^{18}F]-florbetaben) and tau ([^{18}F]-PI2620) accumulation in tandem with separate structural and functional MRI protocols.

Impact: The BrainPET will open new capabilities on existing MRI scanners at UC Davis for dynamic, functional assessment of the brain, and reduce patient scantime while preserving quantitative image accuracy in a broad range of neurological conditions.

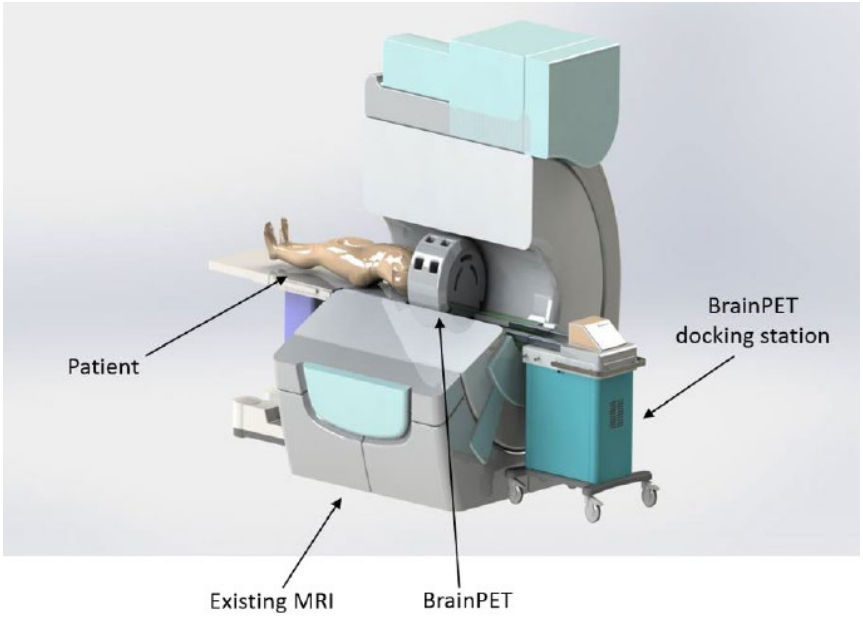

Figure caption: Schematic of the versatile BrainPET insert that integrates with existing whole-body MRI systems to enable high quality, simultaneous PET/MRI brain scans.

Diagnostic and Quality Improvement Insights Enabled by a Comprehensive NLP Pipeline for Radiology and Pathology Reports

Thomas Loehfelm

Department of Radiology, UC Davis

Radiologists and pathologists produce data-rich reports that contain information used by physicians throughout the healthcare system to deliver quality patient care. Most of the data is in plain text and inaccessible to simple queries, which is an obstacle to diagnostic quality improvement initiatives. We have implemented a program called PATHFINDER that applies comprehensive NLP to all radiology and pathology reports enabling accurate radiology-pathology correlation to support education, quality improvement, and diagnostic accuracy assessment. We will review the basic architecture of PATHFINDER and demonstrate its usefulness in measuring radiologist diagnostic accuracy and measuring the impact of clinical decision support on PE detection from the ER.

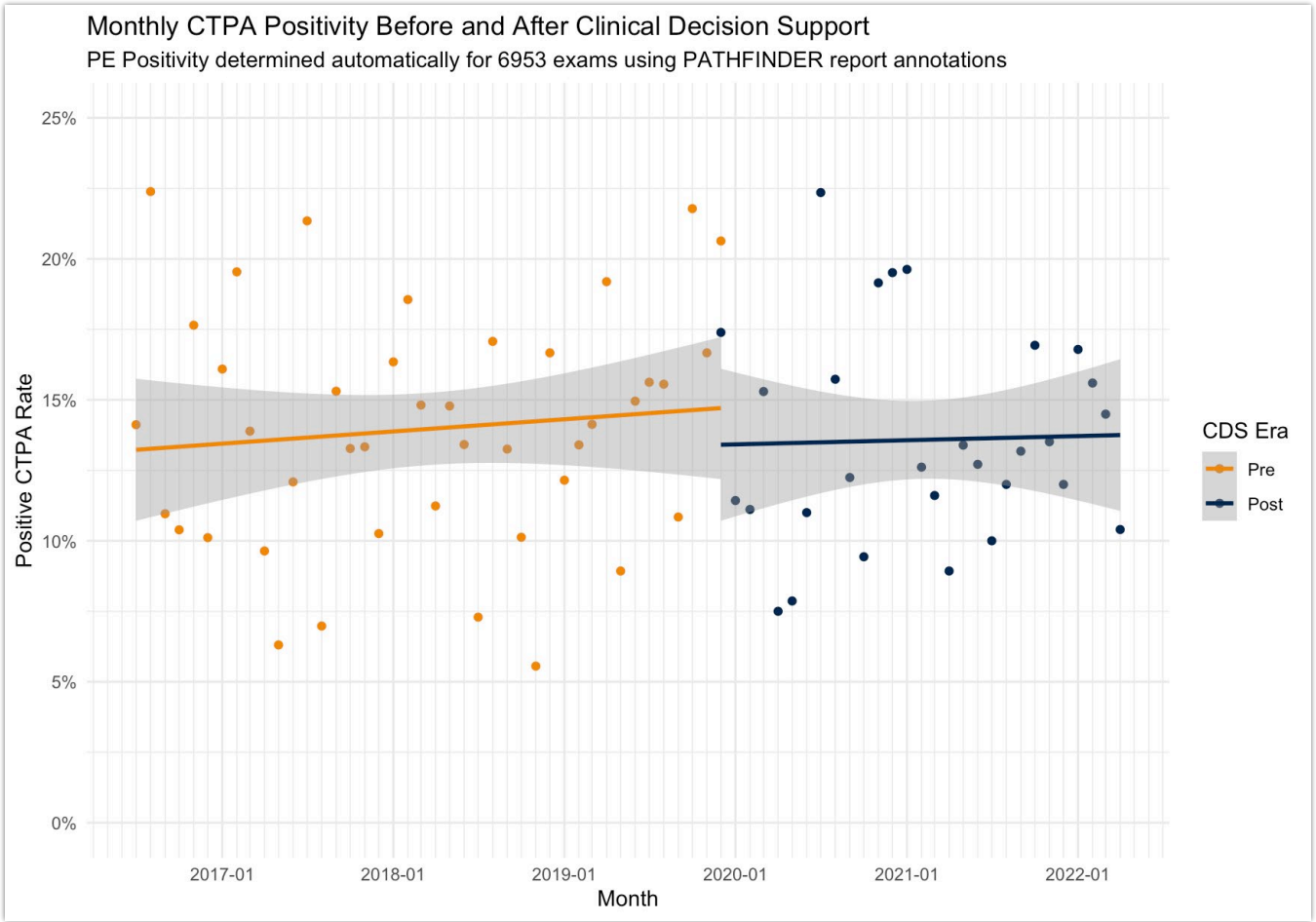

“3D PrintViz” Laboratory: UC Davis’s Medical 3D Printing and Visualization Laboratory

Osama Raslan, Ahmadreza Ghasemiesfe

Department of Radiology, UC Davis

Teaching Points: With the recent advances in the 3D printing technology, more and more medical practitioners have adopted this powerful tool to assist them in delivering individualized high-quality patient care especially for complex and challenging cases.

The aim of this work is to provides an overview of Medical 3D printing at UC Davis, introducing the technology, highlighting the current and potential medical 3D printing applications, and addressing some of the challenges and frequently asked questions about this cutting-edge technology at UC Davis.

***Table of Contents/Outline:**

- Introduction to 3D printing
- 3D printing in Medicine
- 3D PrintViz lab’s Case use examples
- Applications:
    - Education of trainees
    - Education of patients
    - Surgical planning & Simulation
    - Creation of Devices
    - Bioprinting
- Augmented Reality
- Challenges
- Frequently asked questions (FAQs)

INDUSTRY PARTNERSHIPS TO DEVELOP ADVANCED PET SCANNERS

[1.2]Simon R. Cherry, [1.2]Ramsey D. Badawi, [1]Jinyi Qi

[1]Department of Biomedical Engineering, UC Davis
[2]Department of Radiology, UC Davis

Industry-academic partnerships can be critical in moving the field forwards and developing and disseminating next generation imaging technologies. The relationship between UC Davis and United Imaging Healthcare (UIH) is one such example, which has led to two high-profile projects to date, the uEXPLORER total-body PET/CT project and the neuroEXPLORER (NX) project. The goal of this presentation is to briefly review the ingredients for a successful partnership and give an overview of the two projects in which UC Davis plays a leading role.

uEXPLORER PET/CT: This system, the world's first medical imaging device that can capture images from the entire human body simultaneously, was developed under a High-Risk/High-Reward Transformative R01 grant from the NIH in partnership with UIH. The concept and supporting case was developed at UC Davis, with the ultimate realization of the system and its manufacturing taking place at UIH. With its 194 cm long axial field of view, and over 500,000 individual detectors, the uEXPLORER was the most complex PET scanner ever built. The system was installed at UC Davis in 2019, has FDA 510(k) clearance and is in routine clinical and research use. The system has been commercialized and there is an installed base of 13 scanners worldwide.

neuroEXPLORER: Based on the highly successful EXPLORER project, a team that included Yale University, UC Davis and UIH was assembled to develop the world's highest sensitivity brain PET scanner. Major funding was secured from the NIH BRAIN initiative and the system is expected to achieve a spatial resolution < 2 mm and with its high geometric collection efficiency and excellent time-of-flight capabilities, an effective sensitivity ten-fold higher than brain scanners currently in use. The scanner is well on its way to completion (Figure 1). The initial system will be sited at Yale, and the system will be commercialized so that it is available for neuroimaging research across the world.

These two examples show how academic-industry partnerships can successfully design, develop, implement and disseminate new imaging technologies and how UC Davis has played a central role in these activities with respect to advanced PET imaging technology.

Figure 1. Photograph of the high resolution neuroEXPLORER PET scanner currently under construction as part of a NIH BRAIN initiative grant between Yale University, UC Davis and United Imaging Healthcare.

Engaging health disparities in biomedical imaging research

Felipe Godinez

Department of Radiology, UC Davis

Radiology departments provide technically advanced imaging services critical to delivering auspicious patient care. The expectation is that irrespective of factors such as race, socioeconomical status, and cultural background; the benefits of Imaging technology should impact the healthcare of all persons equally. However, studies have found that these factors are associated with health disparities amongst non-white communities.

Health disparities can be met at the level of research through a manifold of actions. One approach is to inspire and mentor young students from underrepresented groups to pursue careers in biomedical sciences with programs at the high school level. In more advanced levels, fostering faculty candidates from minority backgrounds will help bring the issues affecting health disparities to the research forefront. An essential part in gaining the trust and support of the population in favor of these objectives is community engagement. This approach helps develop conversations with low-income communities and introduces them to the benefits of biomedical research. The Radiology Department at UC Davis health is poised to carry out these actions.

Here I show case the community engagement project that was part of the Explorer PET scanner research at UC Davis. Its primary goal was to promote greater inclusiveness of racial/ethnic minorities to benefit from the world's first ever total-body PET scanner (EXPLORER). In collaboration with the Biomedical Technology Program and the Community Advisory Board (UC Davis resources) several media outlets were used to introduce the Explorer scanner to the community. The results were increased participation of minority groups into ongoing clinical trials.

It is research planned with community involvement that will help bring more inclusivity to developing technology with equitable benefits. This will also help dissolve the cultural fears surrounding biomedical research and institutionalized medical care.

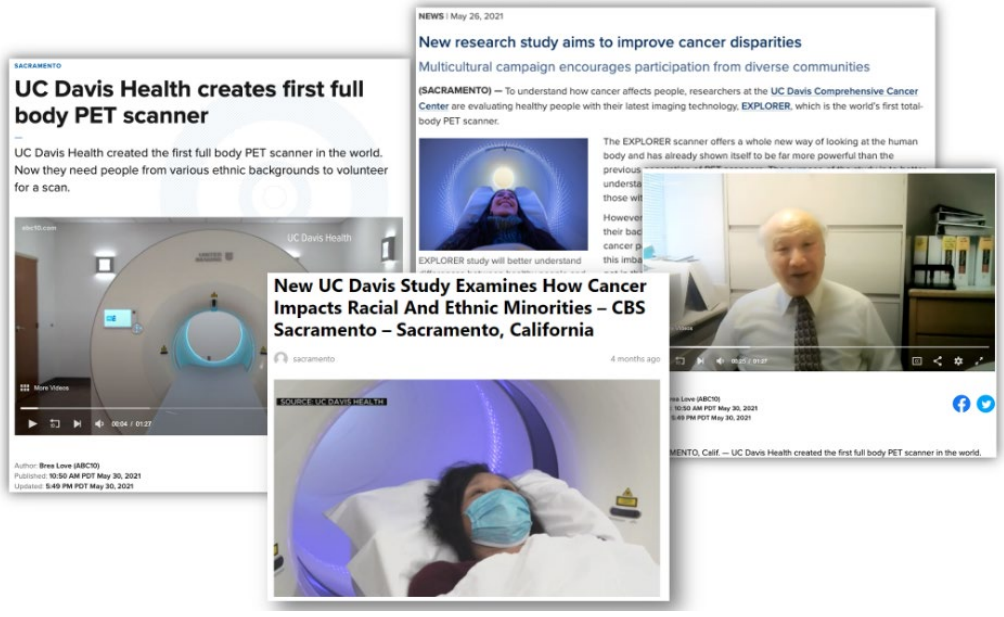

Figure 1 Examples of communications across several media outlets.

High resolution CT for lung nodule characterization: a multi-reader comparison against conventional normal resolution CT

Anthony F. Chen, Mohammad H. Madani, Lorenzo Nardo,
Ahmadreza Ghasemiesfe, Andrew M. Hernandez

Department of Radiology, UC Davis, CA

Purpose: To compare high-resolution CT (HRCT) with conventional CT for lung nodule characterization on the same patient.

Materials and Methods: 24 retrospective chest HRCT scans with pulmonary nodules were collected. Corresponding normal resolution (NR) reconstructions were synthesized using a validated algorithm - facilitating clinical imaging comparisons on the same patient at the prescribed dose. An experienced cardiothoracic radiologist localized each nodule and recorded the density and dimensions. HR and NR datasets for each patient were split and randomly distributed into two reading sessions (separated by a washout period) for two radiologist readers who were blinded to the reconstruction. Evaluation parameters included: lung nodule size (long and short axis), margin clarity (5-point Likert scale: 1=not visible; 2=poor visualization/delineation,3=adequate,4=good,5=excellent), lung nodule density (ground glass, part solid, solid), and density confidence (0-100%). These parameters were evaluated by the readers using a 3D visualization software built in-house with the target nodule locations indicated by a spherical VOI.

Results: Inter-reader agreement was excellent for long and short axis assessment (ICC=0.925 and 9.924, respectively), good for nodule density (k=0.772), and fair for margin clarity (k=0.399). Averaged across readers, margin clarity was rated as 3.21 and 3.00 for HR and NR, respectively. Nodule density was correctly scored for 90% and 94% of HR and NR, respectively. For cases where nodule density was correctly identified, the confidence was the same for reader 1, but for reader two the confidence was on averaged 88% and 85% for HR and NR, respectively. HR resulted in a smaller bias in short axis nodule quantification compared with NR, and the opposite was true for the long axis.

Conclusion: Our initial evaluation of HRCT for lung nodule characterization demonstrated an improved ability to visualize margin clarity and quantify short axis dimensions. Lung nodule size, margin clarity, and density are known features to predict likelihood of malignancy. These findings could improve clinical decision making as it relates to the follow up and diagnostic accuracy of chest HRCT.

Clinical Relevance: This work provides an initial evaluation for HRCT lung nodule characterization utilizing a robust framework for clinical comparisons between high-resolution and conventional CT on the same patient.

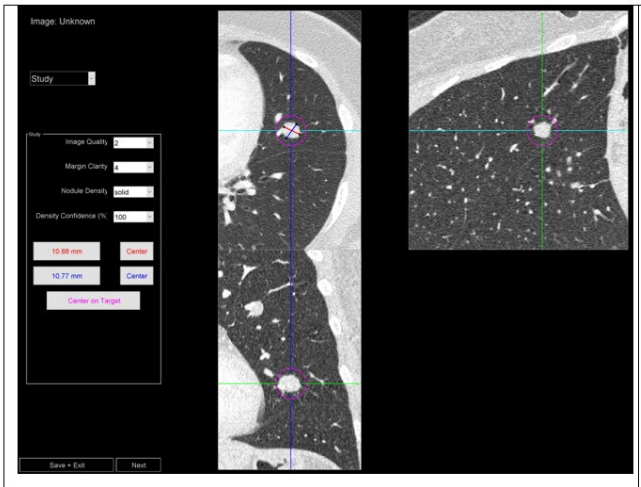

Figure 1A. Custom built visualization software used for the reader study including a GUI for scoring the nodule characteristics

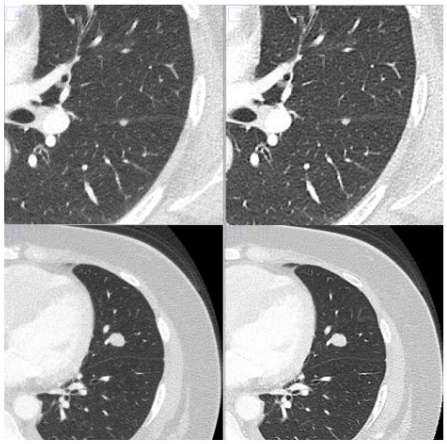

Figure 1B. Examples of two solid lung nodules for high resolution (HR) acquisitions (left column) and the corresponding synthesized normal resolution (NR) images (right column)

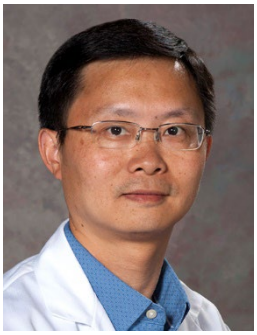

Molecular Imaging of Nonalcoholic Steatohepatitis (NASH): A Collaborative Team Effort at UC Davis Health

[1]Guobao Wang, [2]Victoria Lyo, [3]Karen Matsukuma, [4]Shuai Chen, [1]Michael Corwin, [1]Ramsey D. Badawi, [5]Valentina Medici, [5,1,6]Souvik Sarkar

[1]Department of Radiology, [2]Department of Surgery, [3]Department of Pathology and Lab Medicine, [4]Department of Public Health, [5]Department of Internal Medicine, UC Davis Health, [6]Florida Research Institute

Introduction: Nonalcoholic steatohepatitis (NASH) is the most severe form of nonalcoholic fatty liver disease that affects a large population along with the increasing rate of obesity in both adults and children. NASH is also believed to affect multiple organ systems including the heart, kidney, and brain. However, noninvasive imaging tools to quantify the severity of disease have been very limited in this emerging landscape. We hypothesize that liver inflammation, a diagnostic hallmark that differentiates NASH from simple fatty liver, is associated with change of glucose transport in the liver and extrahepatic organs. To explore this hypothesis, we have built a team of scientists and physicians at UC Davis Health to develop PET molecular imaging tools and apply the tools for clinical study of NASH.

Methods: We developed a parametric PET method that exploits dynamic PET imaging and advanced kinetic modeling to measure glucose transport properties using the widely accessible radiotracer ^{18}F-fluorodeoxyglucose (FDG). The method was tested in patients with biopsy-confirmed fatty liver disease on a conventional PET/CT scanner for assessing liver (60 patients) or on the EXPLORER total-body PET/CT system for total-body multiorgan evaluation (over 20 patients).

Results: Our studies suggest that increased liver inflammation is associated with decreased liver glucose transport rate as measured by parametric PET. This PET biomarker of liver inflammation led to a high accuracy for diagnosing NASH when it is jointly used with a CT-based method for measuring liver steatosis. The technique and clinical evaluation were reported in four peer-reviewed journal papers. Initial results from the total-body PET study suggest changes of glucose transport may also occur in extrahepatic organs, including the brain.

Conclusion: Parametric PET of glucose transport can be a sensitive tool for evaluating NASH. Future directions include new tracer studies (e.g., to image fibrosis), evaluation of intervention (e.g., bariatric surgery), and multicenter studies. These efforts would not be possible without an interdisciplinary team collaboration approach.

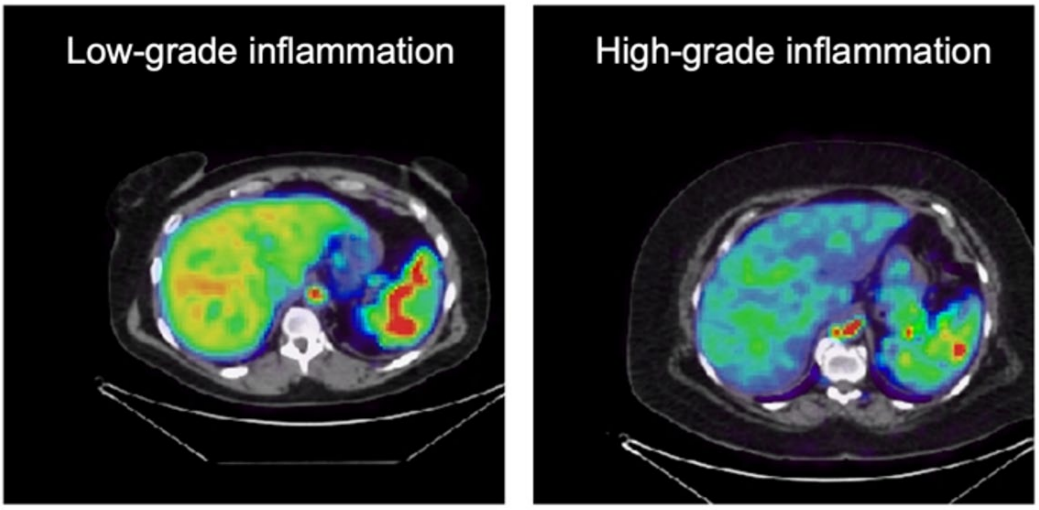

Parametric image of liver blood-to-tissue glucose transport rate

Automated whole brain segmentation of T2w MRI brain scans of rats exposed to organophosphates using a U-Net neural network

[1,2]V. A. Porter, [1,2]B. A. Hobson, [4]B. Foster, [5]P. J. Lein, [2,3]A. J. Chaudhari

[1]Department of Biomedical Engineering, UC Davis, [2]Department of Radiology, UC Davis, [3]Center for Molecular and Genomic Imaging, [4]TechMah Medical LLC, [5]Molecular Biosciences, University of California, Davis

Introduction: Whole brain delineation (WBD) is a common technique used in neuroimaging analysis to remove non-brain signals from brain measures of interest and improve the accuracy of automated co-registration techniques. However, current WBD methods perform poorly on images that show large deformations due to neuropathology, like from organophosphate intoxication (OPI). The 2D U-Net convolutional neural network (CNN) has shown promise for brain MRI segmentation in multiple species. We optimized and evaluated a 2D U-Net CNN for WBD on MRI brain scans from an OPI rat model.

Methods: The CNN had a modified 2D U-Net architecture. We optimized the training parameters and data augmentation functions to improve training accuracy. Our data consisted of T2-weighted MRI brain scans (n=120 scans, voxel size: 125x125x500µm, matrix size: 280x200x59, acquired on a Bruker BioSpec 7T scanner, phased array coil) and matching manually segmented WBD labels. Scans were of adult Sprague Dawley rats from an OPI (diisopropylfluorophosphate (DFP)) study that compared novel therapies (midazolam (MDZ), allopregnanolone (ALO), and MDZ and ALO (DUO)) to untreated, DFP-exposed animals (DFP) and vehicle controls (VEH) across three timepoints (3-, 7-, and 28-days post-OPI). The training and test datasets consisted of 100 scans (DFP=23, MDZ=23, ALO=21, DUO=21, VEH=12) and 20 scans (DFP=4, MDZ=4, ALO=4, DUO=4, VEH=4). MRI scans were preprocessed: N4ITK bias correction, center-cropping (to [200x200x59]), and down sampling (to [128x128x59]). To evaluate CNN performance, Dice coefficients (DC) were calculated between CNN-generated labels and manual segmentations.

Results and Conclusion: The CNN-generated labels achieved a DC (median[range]) of 0.9836[0.9356-0.9900] across all scans, indicating excellent segmentation accuracy. The training runtime was 30 minutes, while application runtime is ~10 seconds/scan. We conclude that a 2D U-Net CNN provided a fully automated, efficient, and accurate segmentation approach. Future research will include examining the applicability of this WBD CNN on other preclinical disease and animal models.

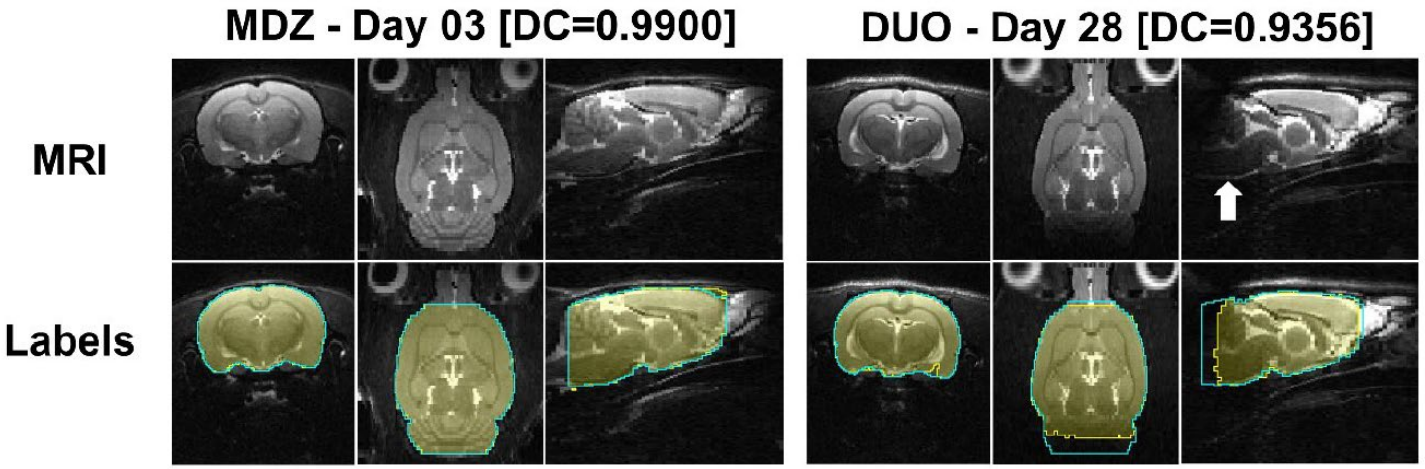

Comparison of scans segmented manually and with the 2D U-Net CNN. **First row**: three orthogonal views of the MRI image of each scan. **Second row:** both manual and CNN labels overlaid on the anatomical scan. The cyan line is the manual segmentation outline, while the yellow region is the CNN output label. The MZD Day 03 scan achieved the highest DC, while the DUO Day 28 scan achieved the lowest DC. The white arrow shows signal loss in the cerebellum that contributes to lower segmentation accuracy.

Effect on Intra-procedural Metrics of Pre-procedural CT Angiography prior to Conventional Angiography in Trauma Patients with Active Extravasation on Initial Portal Venous Phase Imaging

Frank Liou, Ryan Di Geronimo, Sishir Rao, Amol Shah, Eric King, Rex Pillai, R. Torrance Andrews, Catherine Vu, Roger E. Goldman

Department of Radiology, UC Davis

INTRODUCTION: Repeat imaging with CT angiography (CTA) may be obtained in select trauma patients with active contrast extravasation on initial portal venous (PV) imaging to distinguish between arterial and venous etiologies. This study investigates the effect of pre-procedural CTA on intraprocedural angiography metrics.

METHODS: 286 Trauma patients presenting to a Level 1 trauma center between 1/2015 and 10/2021 with a radiology report containing active extravasation on PV abdominopelvic imaging were identified. 75 patients from this cohort subsequently underwent conventional angiography (CA). These patients were divided into those who underwent CTA evaluation prior to CA (CTA+CA, n=42) and those who underwent CA directly (CA only, n=33). Primary outcomes were intra-procedural contrast dose, fluoroscopy time, radiation dose, and sedation time. Secondary outcomes were conventional angiography (CA) findings and embolic therapy method, (i.e., targeted versus empiric).

RESULTS: There was no statistically significant differences in mean intra-procedural sedation time (minutes) (103.5±44.7 vs 107.5±70.2; p=0.777), contrast dose (mL) (121.3±42.7 vs 112.8±68.3, p=0.534), fluoroscopy time (minutes) (15.8±8.7 vs 18.6±17.9; p=0.412), and radiation dose (mGy) (1058.2±1125.7 vs 928.9±1208.8; p=0.637). There was also no significant difference in the percentage of patients who received embolization for active extravasation, patients who received embolization for vessel irregularity, and patients who received empiric embolization in the setting of a normal CA (table 1).

CONCLUSION: While CTA may be a useful tool in identifying patients with true arterial extravasation and minimizing unnecessary arterial intervention in patients with venous bleeding, obtaining CTA imaging prior to CA does not reduce the use of contrast, radiation, and sedation intra-procedurally in our trauma population. The additional data from pre-procedural CTA also does not appear to decrease the rate of empiric embolization compared to those without pre-procedural CTA imaging. The data suggest judicious use of repeat imaging in trauma patients destined for conventional angiography.

Table 1: Angiographic outcomes and intervention

	Angio Only (n=33)	CTA + Angio (n=42)	P=Value
Extravasation with embolization	36.4%	47.6%	0.357
Vessel irregularity with embolization	21.2%	23.8%	>0.999
Vessel irregularity with no intervention	0.0%	2.4%	>0.999
Negative CA with empiric embolization	12.1%	9.5%	0.725
Negative CA with no intervention	30.3%	29.2%	>0.999

CD8-Targeted Total-Body PET Imaging of T Cells in Patients Recovering from COVID-19

[1]Negar Omidvari, [2]Terry Jones, [3]Pat M Price, [2]Fatma Sen, [4]Barbara Shacklett, [5]Stuart Cohen, [1,2]Ramsey D Badawi, [6]Ian Wilson, [1,2]Simon R. Cherry

[1]Department of Biomedical Engineering, UC Davis, [2]Department of Radiology, UC Davis, [3]Department of Surgery and Cancer, Imperial College, London, United Kingdom, [4]Department of Medical Microbiology and Immunology, School of Medicine, UC Davis, [5]Department of Internal Medicine, UC Davis, [6]ImaginAb, Inc., Inglewood, CA

Background: CD8+ T cells are key players in immune response. Following viral infection or vaccination, a small portion of antigen-specific T cells differentiate into memory cells, forming a long-term protective memory against reinfection. However, in vivo information about COVID-19-specific T cell immunity is limited, since 95% of T cells are not in the circulation and tissue sampling has been minimal. This pilot study aims to provide an *in vivo* measure of tissue distribution of CD8+ T cells after COVID-19 infection, using total-body imaging of a labeled minibody with high affinity to human CD8.

Materials and methods; 5 COVID-19-recovered patients and 3 healthy controls were studied. Subjects received ~0.5 mCi of ^{89}Zr-Df-Crefmirlimab-Berdoxam and had 60-min total-body PET/CT scans at 6-h and 48-h post-injection. Control subjects and 3 COVID-19 patients had an additional 90-min dynamic scan. Scans of 3 COVID-19 patients were repeated after 4 months. Volume-of-interest were drawn on spleen, liver, lungs, bone marrow, lymph nodes, tonsils, and blood-pool. Two-tissue compartmental modelling was performed on the dynamic data to derive $K_i = \frac{K_1 k_3}{k_2+k_3}$ and $V_T = \frac{K_1}{k_2}\left(1+\frac{k_3}{k_4}\right)$.

Results: In all subjects, activity decrease in bone marrow and spleen between 6–48 h was observed with parallel activity increase in lymph nodes and tonsils, suggesting cell-trafficking (Figure 1). Tissue-to-plasma ratio (0–7 h), Ki, and V_T were higher in bone marrow of the COVID-19 patients than controls and were the highest in one COVID-19 patient, infected twice with the virus.

Conclusions: Total-body imaging of CD8+ T cells with sub-millicurie levels of ^{89}Zr-labeled tracer resulted in the ability to quantify rates of uptake and concentrations of the tracer in lymphoid tissues throughout the body, along with T cell migration over a 48-h period. Current data suggest that the bone marrow T-cell pool in COVID-19-recovered patients is larger or has increased CD8 expression compared to controls.

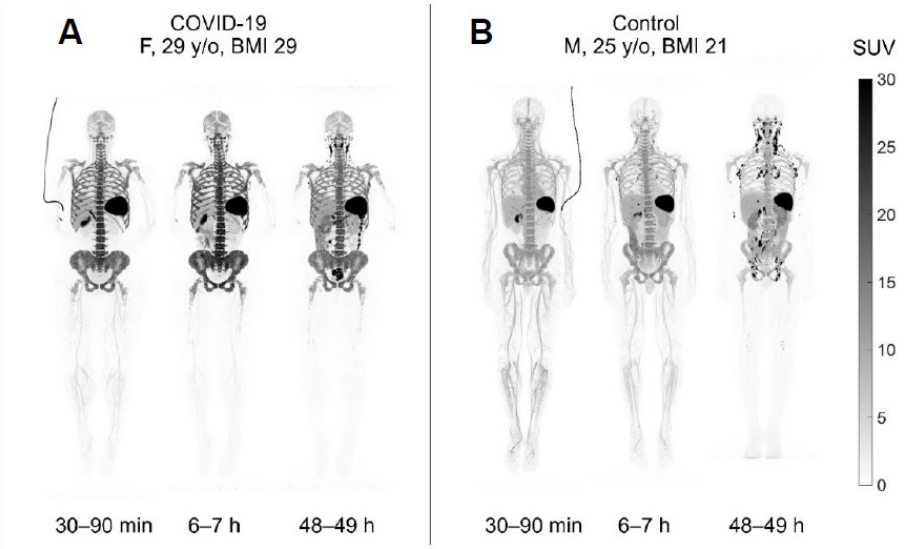

Figure 1. Example SUV maximum intensity projections of (A) a recovered COVID-19 patient, compared to (B) a healthy subject scanned on the uEXPLORER at three timepoints. Increase in lymph node uptake and decrease in bone marrow and spleen uptake is observed between 6 h and 48 h imaging time points.

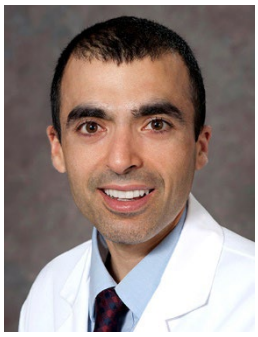

Meniscus MRI

[1]Cyrus Bateni, [2]Christopher Holland, [1]Dillon Chen, [2]Cassandra Lee

[1]Department of Radiology, UC Davis, [2]Department of Orthopedic Surgery, UC Davis

Introduction: Historically, magnetic resonance imaging (MRI) results have been used to identify a meniscal tear, with the intra-operative findings dictating whether a meniscal repair could be performed. Our goal was to analyze whether MRI can be used to reliably predict if a meniscal tear is repairable, which would enhance patient care by managing treatment expectations pre-operatively.

Methods: We retrospectively identified patients who underwent a meniscectomy or meniscal repair and imaging at a UC Davis between 2010 and 2018 and in whom there was an MRI within 3 months of surgery. 193 patients (203 exams) were included in the analysis; imaging review was completed by three blinded reviewers – 2 musculoskeletal radiologists and 1 orthopedic surgeon. Previously validated arthroscopic criteria were used to score on MRI the repairability of a meniscal tear on a scale of zero to four, with one point awarded for each of the following – tear within 4 mm of the meniscosynovial junction, tear longer than 10 mm, intact inner meniscal segment, and a tear of >50% thickness. Tears with a score of 4 were predicted to be repairable.

Results: 134 underwent meniscectomies and 68 underwent meniscal repair. The radiologists (κ=0.08, κ=0.35), and orthopedic surgeon (κ=0.44) showed poor and moderate correlation, respectively, in identifying repairable meniscal tears. When analyzed independently, type and nature of tears did not increase the ability to predict repairability.

Conclusion: Using MRI based upon established arthroscopic criteria to predict the repairability of meniscal tears was not effective. Further investigation is needed.

High-grade pediatric renal trauma: prognostic value of ureteral contrast

[1]Phillip J Kim, [1]Hansen T Lui, [2]Lisa H Kang, [3]Blythe P Durbin-Johnson, [4]Eric A Kurzrock

[1]Department of Urologic Surgery, UC Davis, [2]Department of Radiology, UC Davis, [3]Public Health Services, UC Davis, [4]Department of Urology, UC Davis

INTRODUCTION: Although non-operative management is encouraged for children with low-grade renal injury, there are no universally accepted guidelines for management of high-grade injury. We sought to determine if any patient variable, in particular the presence of contrast in the ureter on delayed images, was associated with intervention.

METHODS: A retrospective review of pediatric patients presenting with grade IV or V renal injury between 2003 and 2021 at a Level 1 trauma center was performed. Renal injury grade was verified and updated, if necessary, based upon the 2018 American Association for the Surgery of Trauma (AAST) injury scale. In addition, we determined if the injury was vascular or collecting system or both. Multivariable logistic regression analyses were performed.

RESULTS: Seventy-five patients (mean age 12.4 years old) with Grade IV (n=53) or Grade V (n=22) injury were identified. Twenty-five patients (33%) had immediate renal intervention within 24 hours of admission, whereas 50 patients were observed. The mean age of observed patients was 11.2 years of age and 15 (30%) had intervention. Delayed images on CT showed ureteral contrast was present in 44 (88%) of observed patients. Multivariable analysis demonstrated that presence of contrast in the ureter is associated with significantly lower odds of intervention, OR 0.06 [0.004-0.456, 95% CI, ($P < 0.01$)].

DISCUSSION/CONCLUSIONS: After high-grade renal injury in children, the presence of contrast in the ureter on delayed CT imaging is associated with lower odds of procedural intervention. Despite the large size, this study is limited by the retrospective nature. After grade IV or V renal injury, presence of ureteral contrast may suggest a less severe renal collecting system defect and better odds that intervention can be avoided.

Table 1: Logistic Regression Analyses of Any Intervention by Patient and Imaging Characteristics

Variable	Multivariable Analysis	
	Odds Ratio (95% CI)	P-Value
Contrast in Ureter: Yes vs. No	0.063 (0.004, 0.456)	0.00497
Injury: Collecting System vs. Vascular	1.799 (0.301, 18.79)	0.53860
Injury: Both vs. Vascular	1.452 (0.161, 18.104)	0.74099
Injury Mechanism: Penetrating vs. Blunt	2.687 (0.197, 28.466)	0.42004
Age (Years)	0.979 (0.827, 1.164)	0.80182
Non-Renal AIS Score	0.858 (0.555, 1.252)	0.43835

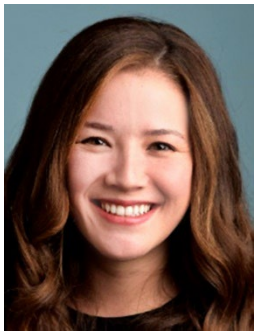

Total-body perfusion imaging using [^{11}C]-butanol

[1]Elizabeth Li, [1,2]Benjamin A. Spencer, [2]Yasser Abdelhafez, [3]Javier Lopez, [2]Guobao Wang, [1,2]Simon R. Cherry

[1]Department of Biomedical Engineering, UC Davis, [2]Department of Radiology, UC Davis, [3]Department of Cardiovascular Medicine, UC Davis

Introduction: Tissue and organ perfusion is critically important in many pathologies. With total-body (TB-)PET we can quantitatively measure tissue and organ perfusion across the entire human body for the first time. Compared to commonly used perfusion tracers such as [^{15}O]-water and [13N]-ammonia, [^{11}C]-butanol has superior first pass extraction fraction across a very wide range of perfusion values. Here, we present the initial methods, dosimetry, and kinetic analysis of an ongoing study assessing the use of [^{11}C]-butanol for dynamic perfusion imaging across the entire body with TB-PET.

Methods: Seven subjects (6 healthy volunteers and 1 patient with peripheral arterial disease) were recruited into this IRB-approved study and gave written informed consent. At each visit, the subjects received an intravenous bolus injection of ~300 MBq of [^{11}C]-butanol and underwent a 30-minute dynamic acquisition at rest. Whole-organ regions of interest (ROIs) were delineated in tissues using PMOD. Dosimetry estimates were performed using OLINDA 2.0 and the MIRD method. In order to estimate regional perfusion (K_1, ml/min/ml), the first 4 minutes were used to perform 1-tissue compartment modeling using the descending aorta as the image-derived input function and joint estimation of bolus delay. Parametric images were generated using the same approach voxel-by-voxel but with the Akaike Information Criterion used to perform model selection.

Results: The average total effective dose was ~3.65 μSv/MBq. As shown by the K_1 maximum intensity projection images (MIPs) in Figure 1, repeat scans demonstrated similar flow estimates. In the patient with PAD, local changes in perfusion were observed using the contralateral limb as a control.

Conclusions: Quantitative dynamic total-body perfusion studies with [^{11}C]-butanol have been performed for the first time in humans. Further subject and patient recruitment will provide an estimate of the reliability and sensitivity of [^{11}C]-butanol parametric imaging using high-sensitivity high-spatial resolution total-body PET.

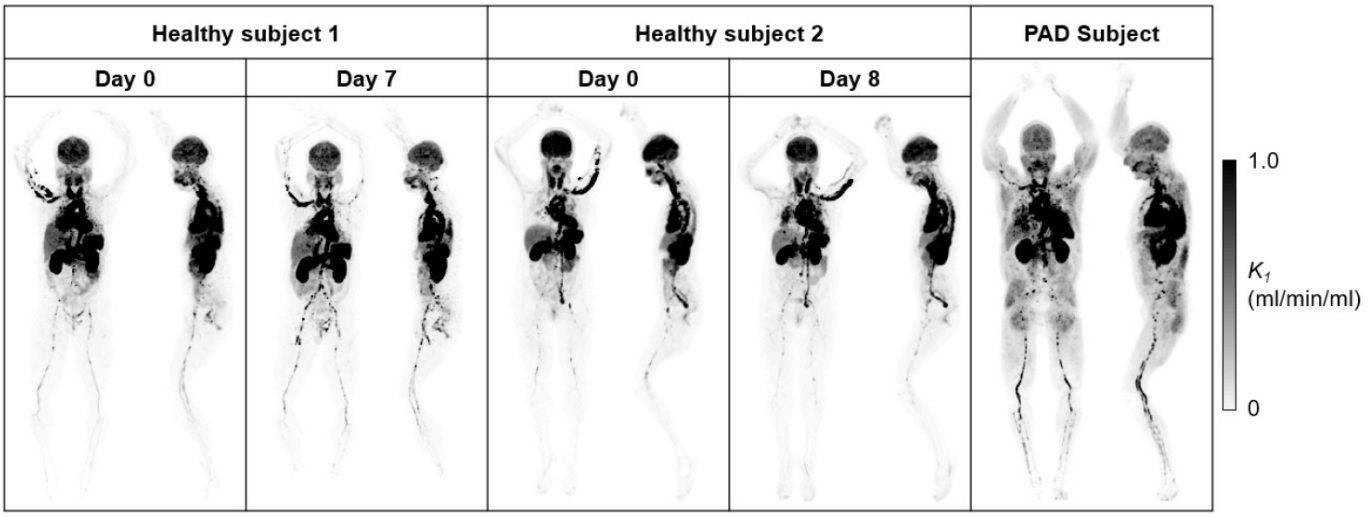

Figure 1. Maximum intensity projection (MIP) of K_1 (perfusion) for the first five acquisitions of the study.

AI-based Automated Lipomatous Tumor Segmentation in MR Images

[1]Quinn Kwan-Tai Ng, [2,9]Chih-Chieh Liu, [1]Yasser G Abdelhafez, [1]S. Paran Yap, [3]Francesco Acquafredda, [2]Silvia Schirò, [1]Andrew L. Wong, [1]Dani Sarohia, [1]Cyrus Bateni, [4]Morgan A. Darrow, [5]Michele Guindani, [5]Sonia Lee, [6]Michelle Zhang, [7]Ahmed W. Moawad, [7]Layla Shere, [7]Khaled M. Elsayes, [8]Roberto Maroldi, [2]Thomas M. Link, Jinyi Qi, [1]Lorenzo Nardo

[1]Department of Radiology, UC Davis, [2]Department of Radiology and Biomedical Imaging, UC San Francisco, [3]Radiologia Pediatrica - Ospedale dei Bambini, ASST Spedali Civili, Brescia, Italy, [4]Department of Pathology and Laboratory Medicine, UC Davis, [5]Department of Statistics, UC Irvine, [6]Department of Diagnostic Radiology, McGill University Health Center, Montreal, Canada, [7]Department of Diagnostic Imaging, University of Texas MD Anderson Cancer Center, Houston, TX, USA, [8]Scienze Radiologiche, Università degli Studi di Brescia, Brescia, Italy, [9]Canon Medical Research USA, Inc.

Diagnostic aids from quantitative radiomics have shown promising results for the characterization of many diseases. However, the extraction of radiomic features for complex structures/diseases such as lipomatous tumors from MRI images remains challenging. This is mainly due to the labor intensive, and error prone identification and segmentation of these tumors needed for accurate analysis. Deep learning (DL) has been proposed for the automation of medical image segmentation to improve accuracy, consistency, and efficiency; however, a major challenge of this task is data heterogeneity from multicenter data for pre-processing algorithms. We aimed to develop and study a DL-based Super Learner (SL) ensemble framework approach in comparison to any single trained neural network.

Pathologically proven LTs on pre-operative T1-weighted/proton-density MR images of 185 patients (4 centers, 20 MR scanners; 102 females; age 58.4±11.9 yrs) were manually segmented and categorized by tumor locations as distal upper limb (DUL), distal lower limb (DLL), proximal upper limb (PUL), proximal lower limb (PLL) or Trunk (T) and grouped by 80%/9%/11% for training, validation, and testing. Six configurations of correction/normalization were applied to data for 5-fold-cross-validation trainings, resulting in 30 base learners (BLs). A SL was obtained from the BLs by optimizing SL weights and performance was evaluated by dice-similarity-coefficient (DSC), sensitivity, specificity and Hausdorff distance (HD95). For predictions of the BLs, the average DSC, sensitivity and specificity from the testing data were 0.72±0.16, 0.73±0.168 and 0.99±0.012, respectively, while for SL predictions were 0.80±0.184, 0.78±0.193 and 1.00±0.010. Average HD95 of the BLs were 11.5 (DUL), 23.2 (DLL), 25.9 (PUL), 34.7 (PLL) and 49.4 (T) mm, whereas of SL were 1.7, 8.4, 15.9, 2.1 and 37.9 mm, respectively.

The proposed method could improve the segmentation accuracy and mitigate the performance instability and data heterogeneity aiding the differential diagnosis of LTs in real clinical situations.

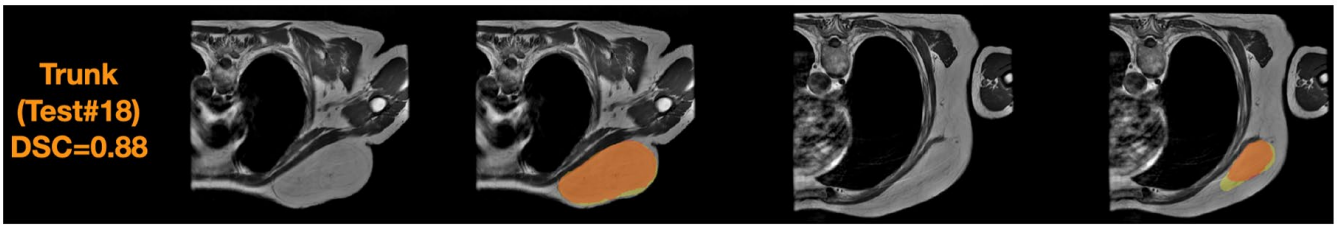

Figure 1: Example SL ensemble predictions (red) and tumor delineations (yellow) per tumor location overlaid on the T1-weighted MR images giving orange color for the correctly predicted tumor region. First two columns represent the central image slices of the tumors without and with the delineations and predictions, respectively, whereas the second two columns represent the edge image slices of the tumors. The predictions are often worse in the edge slices than in the central slices of tumor.

First-in-human imaging and dosimetry of novel integrin [^{18}F]$\alpha_v\beta_6$ binding peptide in patients with metastatic carcinoma

[1]Cameron C. Foster, [2]Sven H. Hausner, [3]Ryan A. Davis, [2,3]Julie L. Sutcliffe

[1]Department of Radiology, UC Davis, [2]Department of Hematology Oncology, Department of Internal Medicine, UC Davis, [3]Department of Biomedical Engineering, UC Davis

Introduction: The goal of this study was to evaluate the biodistribution and dosimetry of an integrin avb6-binding peptide ([^{18}F]avb6-BP) for the noninvasive imaging of a diverse range of malignancies with PET.

Methods: Patients with a prior diagnosis of either metastatic lung, colon, breast, or pancreatic cancer were enrolled. Each patient received a maximum injected dose of 10 mCi of [^{18}F]αvβ6-BP. PET/CT Imaging was performed at four time points (30, 60, 120, 180 minutes post injection) with ultra low dose CT at 30, 120, and 180 min, and low dose at 60 min. Regions of interest were drawn at all time points for representative organs and tissues using a GE Advantage workstation or Server. Decay corrected clearance curves and biodistribution models were generated for all drawn regions. Dosimetry data were calculated using OLINDA 1.1 software.

Results: Between December 2016 and January 2020, 26 eligible patients (11M, 15F ages 39-78) were enrolled. [^{18}F]αvβ6-BP was predominantly renally excreted with highest radioactivity in the kidneys and bladder (from excretion) followed by the gastrointestinal tract. Minimal radioactivity was seen in the normal brain, lungs, liver, heart, vascular system and bone marrow. Furthermore, sub-centimeter metastases to these organs were detected. The mean effective dose for [^{18}F]αvβ6-BP was 0.717 mSv/mCi.

Discussion: [^{18}F]αvβ6-BP was predominantly renally excreted and [^{18}F]αvβ6-BP PET/CT imaging can detect both primary tumors and metastases. The biodistribution was reproducible and predictable. The degree of radioactivity seen in lesions between similar tumor types varied by size; it was superior to standard tracer agents such as [^{18}F]fluorodeoxyglucose ([^{18}F]FDG) (Figure).

Conclusion: Imaging using [$_{18}$F]$\alpha_v\beta_6$-BP has an immediate clinical benefit for the detection of multiple tumor types. Dosimetry values for [$_{18}$F]$\alpha_v\beta_6$-BP are comparable to those for other standard PET imaging agents.

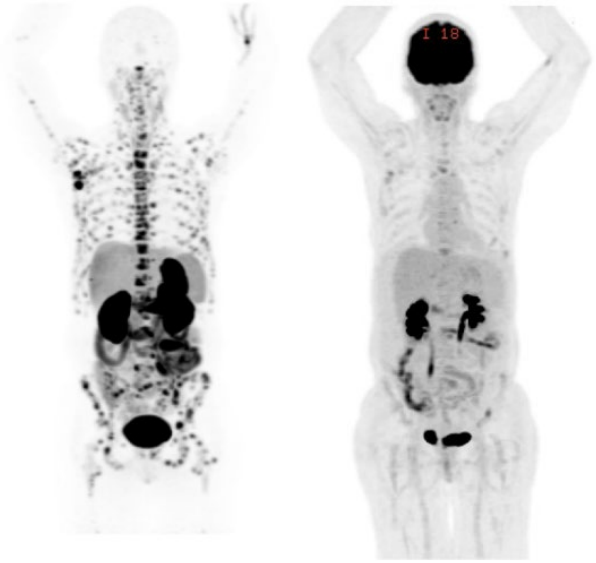

Sutcliffe et. al, Visualizing Cancer. Cancer Cell. 2020 Dec 14;38(6):753-756. doi: 10.1016/j.ccell.2020.11.014

Figure: 56 yo female with history of ER+ / HER2- (BRCA 1&2 negative) breast cancer status post bilateral mastectomy and multiple chemotherapy regimens for multiple recurrences. (Left) [^{18}F]αvβ6-BP PET/CT imaging (SUV max scale 15) revealed diffuse, intense osseous lesions throughout the axial and appendicular skeleton and in multiple right axillary and cervical lymph nodes. (Right) Follow-up [^{18}F]FDG PET/CT one week later (SUV max scale 7) showed very little uptake in the osseous or lymph nodes of the right axilla.

Poster Abstracts

Characterization of Enthesitis Burden in Psoriatic Arthritis using Total-Body PET/CT Imaging with the ^{18}F-FDG radiotracer	Yasser G. Abdelhafez
^{18}F-Fluciclovine PET Uptake in Thumb Carpometacarpal Joint: Initial Observations	Yasser G. Abdelhafez
Sympathetic Ganglia are More Frequently Visualized on 68Ga-Dotatate Total-Body PET/CT Imaging	Yasser G. Abdelhafez
Diversifying the Subject Cohorts in Total-Body PET Research: A Feasibility Study	Ramsey D. Badawi
Validation and Optimization of a Scatter Correction Method for Total-Body Positron Emission Tomography	Reimund Bayerlin
^{18}F-FDG Gallbladder Uptake: Observation from a Total-Body PET/CT Scanner	Anna Calabro
Using total body PET to elucidate whole-body metabolism in the tissue-specific level	Maria Chondronikola
Quantitative T_2 mapping as a biomarker of neuropathology resulting from acute organophosphate intoxication in a rat model	Alita Jesal D'Almeida
A Monte Carlo analysis of Guidewire Safety Comparing a Body and Local coil	Felipe Godinez
Non-invasive quantification and SUVR validation of [^{18}F]-florbetaben with total-body EXPLORER PET	Emily N. Holy
Pediatric Intranodal CT Lymphangiography with Water-Soluble Contrast Media	Zachary B. Jenner
The Effect of Co-Axial Incisions on the Traction Removal Force of Mushroom-Retained Gastrostomy Tubes	Abdullah Khan
Lesion Detectability in Contrast-Enhanced Breast CT using Model Observers	Su Hyun Lyu
Utilization of EOS™ Imaging for Evaluation of Bowel Management and Radiation Dose Reduction	Rebecca Stein-Wexler
Interstitial Space Properties of ^{18}F-fluorodeoxyglucose in Nonalcoholic Fatty Liver Disease	Quyen Tran
Management of Incidental Findings At The EXPLORER Molecular Imaging Center	Ofilio Vigil
Open Kinetic Modeling Initiatives to Accelerate Quantitative Molecular Imaging Research at UC Davis and in the International Community	Guobao Wang
Multi-organ metabolic changes in COVID-19 recovery measured with total-body dynamic ^{18}F-FDG PET	Yiran Wang
Cross-validation log-likelihood regularization strength optimization in penalized likelihood reconstructions for total-body and conventional PET	Qian Wang
Kernel SIME: simultaneous estimation of blood input function using a kernel method and its evaluation with total-body PET	Yansong Zhu

Characterization of Enthesitis Burden in Psoriatic Arthritis using Total-Body PET/CT Imaging with the ^{18}F-FDG radiotracer

[1]Yasser G. Abdelhafez, [2]Siba P. Raychaudhuri, [1]Dario Mazza, [1,3]Benjamin Spencer, [1]Lorenzo Nardo, [1,3]Simon R. Cherry, [1,3]Ramsey D. Badawi, [1]Abhijit J. Chaudhari

[1]Department of Radiology, [2]Department of Internal Medicine/Rheumatology, [3]Department of Biomedical Engineering, University of California - Davis, CA, USA

INTRODUCTION: Inflammation at sites of tendon and ligament attachment (enthesitis) could represent a disease hallmark in psoriatic arthritis (PsA) patients. We explored utility of high-sensitivity Total-Body (TB) 18F-FDG PET/CT imaging for the characterization of enthesitis burden in PsA patients.

METHODS: This ongoing work prospectively recruited 15 participants (14 male, 1 female; mean age of 56.8±16.3 years), with established diagnosis of PsA. All subjects underwent full rheumatological evaluation including Leeds enthesitis index (LEI) and TB-PET/CT with 77.7±4.7 MBq of ^{18}F-FDG. Qualitative and quantitative findings of 38 entheses per participant (38x15=570) were assessed. The evaluated entheses were derived from 6 different enthesitis outcome measures (LEI, San Francisco, MASES, MAJOR, SPARCC, and 4-Point enthesitis measures). Each enthesis was visually and quantitatively evaluated (rSUVmax=SUVmax/blood pool SUVmean).

RESULTS: PET/CT was positive in 127/543 evaluable enthesis (23.4%) from 14 out of the 15 participants. On rheumatologic examination and PET/CT, respectively, 7 and 21 out of 82 evaluable LEI entheses were positive. PET/CT was positive in 5/7 tender entheses and detected inflammation in 16 more LEI entheses. Components of SPARCC and San Francisco measures demonstrated the highest absolute number of positive entheses (66 and 59, respectively). However, components of LEI were the most active **(Figure 1)** with summed rSUVmax of 14.1±9.8 compared to 8.0±5.1and 7.0±4.8 for SPARCC and San Francisco measures, respectively.

DISCUSSION: Current clinical measures of enthesitis, based on clinical examination, are driven by anatomical site accessibility rather than actual disease burden. The mismatch between clinical and ^{18}F-FDG findings substantiates that PET could detect subclinical entheseal inflammation. On the other hand, tenderness alone might not be always indicative of active inflammation. Accurate quantification of systemic burden of enthesitis could be useful for better stratification of disease extent and severity.

CONCLUSION: Evaluation of enthesitis burden on total-body 18F-FDG PET/CT scans is feasible in patients with psoriatic arthritis.

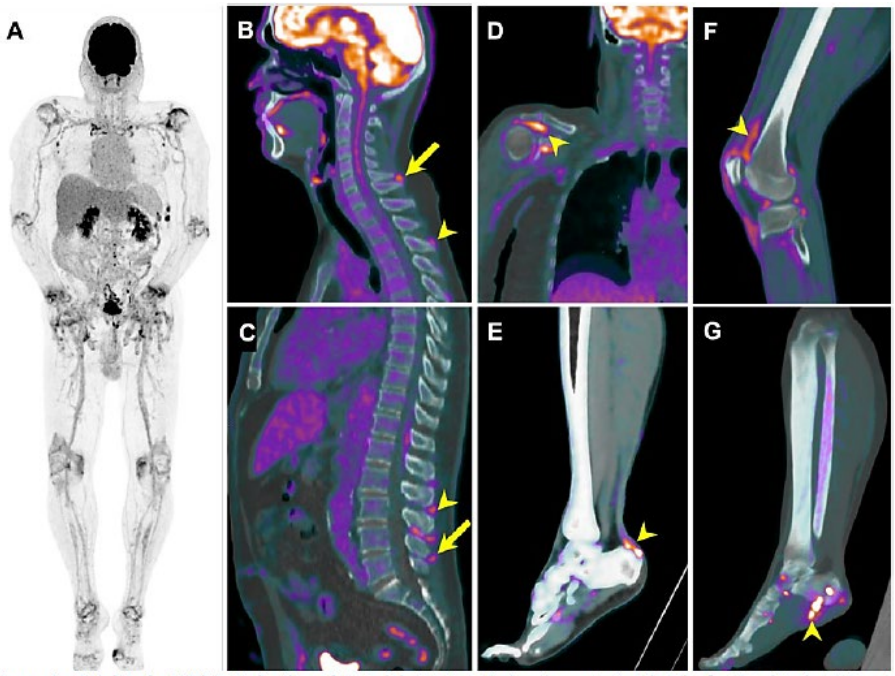

Figure 1 . Total-Body PET/CT Evaluation of PsA: (A) Maximum-intensity projection (MIP) of a Total-Body PET scan demonstrating multiple active joints (shoulders, sternoclavicular joints, elbows, wrists, knees, ankles, left first MTP). Fused PET/CT images from different participants demonstrating enthesitis patterns throughout the body (B-G). The spine entheses are involved at the cervical (B, arrow at C7 and arrowhead at T3), and lumbar regions (C, arrow at L5 and arrowhead at L3/L4/L5 inter/supra-spinous ligaments). Other inflamed entheses include right supraspinatus (D), Achilles (E), and patellar tendons (F), and plantar fascia (G).

^{18}F-Fluciclovine PET Uptake in Thumb Carpometacarpal Joint: Initial Observations

[1]Yasser G. Abdelhafez, [1]Lorenzo Nardo, [1,2]Simon R. Cherry, [1,2]Ramsey D. Badawi, [1]Abhijit J. Chaudhari

[1]Department of Radiology, [2]Department of Biomedical Engineering, UC Davis

INTRODUCTION: Thumb carpometacarpal (CMC) joint osteoarthritis (OA) is a common yet poorly understood condition with high prevalence in the older population[1]. Altered joint amino acid (AA) metabolism has been hypothesized to contribute to OA pathogenesis[2,3]. Among the AAs, glutamine was shown to be deficient in the synovial fluid of OA joints[2,3]. ^{18}F-Fluciclovine is a synthetic AA that behaves in vivo like glutamine[4]. In this work, we evaluated the frequency of detecting thumb CMC abnormality on ^{18}F-Flucicoclovine PET/CT scans.

METHODS: We included men with prostate cancer who underwent standard-of-care ^{18}F-Fluciclovine total-body PET/CT scans for evaluation of biochemical recurrence and/or disease extent. Images were read for any abnormal uptake at the thumb CMC joint. The CT portion of the study was reviewed for structural changes of osteoarthritis; accordingly, Eaton-Littler Stage between I & IV was assigned for each joint.

RESULTS: A total of 28 scans were deemed evaluable (28 patients, mean age 73±9 yrs). On PET, 24 joints from 17 patients showed abnormal ^{18}F-Fluciclovine uptake (Table under Figure 1A, Top). Concordance between PET and CT was seen in 42 joints (25 negative, 17 positive). PET was positive in 7 joints that were negative on CT for OA (Figure 1B) while CT was positive in 7 joints that showed no abnormal uptake on PET images.). SUVmax showed moderate positive correlation with Eaton Littler stage **(Graph under Figure 1A, Bottom).**

DISCUSSION: The elevated ^{18}F-Fluciclovine uptake in an OA joint may indicate glutamine deficiency, hence T-cell activation, a bellwether for downstream joint degeneration[3]. Administration of glutamine has suppressed OA progression in a rat model, and supplementation of glutamine could provide a novel therapeutic approach to OA3.

CONCLUSION: ^{18}F-Fluciclovine total-body PET/CT scans show accumulation of the ^{18}F-Fluciclovine radiotracer in thumb CMC joints with OA. The uptake intensity showed a moderate correlation with Eaton-Littler OA stage.

REFERENCES:

1. Ladd AL, et al. *Instr Course Lect*. 2013;62:165-179.
2. Akhbari P, et al. *Bone Jt Res*. 2020;9(3):108-119.
3. Zheng K, et al. *J Orthop Res*. 2017;35(9):1973-1981.
4. Oka S, et al. *Mol Imaging Biol*. 2014;16(3):322-329.

Figure 1A

PET Fluciclovine Uptake

CT Findings	Negative	Bilateral	Unilateral	Total
Negative	***8***	2	2	12
Bilateral	2	***4***	2	8
Unilateral	1	1	***6***	8
Total	11	7	10	28

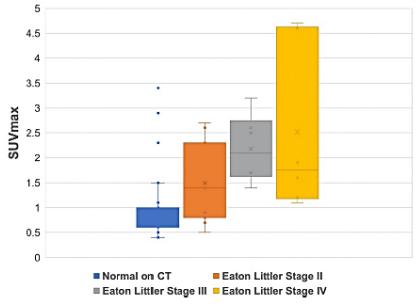

Figure 1A: (Top) Table showing the frequency of abnormal findings on ^{18}F-Fluciclovine PET and CT on per patient-basis. **(Below):** Boxplots of PET SUV_{max} for different Eaton-Littler stages of thumb CMC OA.

Figure 1B: Example images of abnormal ^{18}F-Fluciclovine uptake from two different patients (shown as PET/CT MIP (left column), CT only MIP (middle column) and cross-section from CT (right column). Top images show CT changes (narrowing & sclerosis) while bottom images demonstrate radial subluxation but no structural damage on CT.

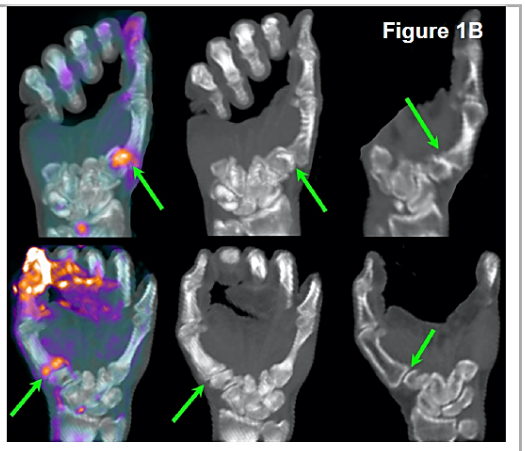

Sympathetic Ganglia are More Frequently Visualized on 68Ga-Dotatate Total-Body PET/CT Imaging

[1]Yasser G. Abdelhafez, [1,2]Elizabeth K. A. Triumbari, [1,3]Anna Calabro, [1]Lorenzo Nardo

[1]Radiology, University of California - Davis, CA, USA, [2]Fondazione Policlinico Universitario A. Gemelli IRCCS, Rome, Italy, [3]University of Brescia and ASST Spedali Civili di Brescia, Brescia, Italy

INTRODUCTION: 68Ga-Dotatate uptake has been frequently seen in the stellate (cervico-thoracic) sympathetic ganglia[1]. However, the relative frequency and uptake intensity of the other common sympathetic ganglia was not previously reported. In this work, we describe the frequency of visualization and uptake intensity of the ganglia on total-body EXPLORER scans comparted to standard conventional scanners.

METHODS: A total of 27 patients (19 women, 8 men, mean age 59.4±14.3) were included. The 27 patients underwent 88 scans (44 scans on each scanner). Scans were randomly and independently evaluated. Three pairs of sympathetic ganglia were qualitatively evaluated (stellate, celiac and sacral) for each scan (total: 264 sites). SUVmax was measured for any visualized ganglion. Background was measured on ascending aorta blood pool (BP) and the ganglia SUVmax ratio to BP was considered as the target-to-background ratio (TBR).

RESULTS: The overall visualization of ganglia was significantly more frequent on EXPLORER compared to GE690. EXPLORER detected 109 ganglia out of 264 sites (41%) compared to 53 (20%) for GE690 (OR: 4.1, 95%CI: 2.4-7.3; P < 0.0001). The difference was still highly significant on site-basis for stellate (n= 72 vs. 38) and celiac (n = 24 vs. 2) but not for sacral ganglia (13 ganglia for each). TBR was significantly higher on EXPLORER compared to GE690 (2.1±1.2 vs. 1.7±1.0; P=0.002).

DISCUSSION: The described sympathetic ganglia are anatomically close to structures that could be involved by various neuroendocrine tumors (e.g., lymph nodes, paragangliomas…etc.). Though physiologic, tracer uptake in these ganglia could be intense on EXPLORER and should not be mistaken for a pathology unless supported by other findings.

CONCLUSION: Sympathetic ganglia are more frequently and conspicuously seen on 68Ga-dotatate EXPLORER scans compared to a conventional scanner. This uptake should not be mistaken for anomaly.

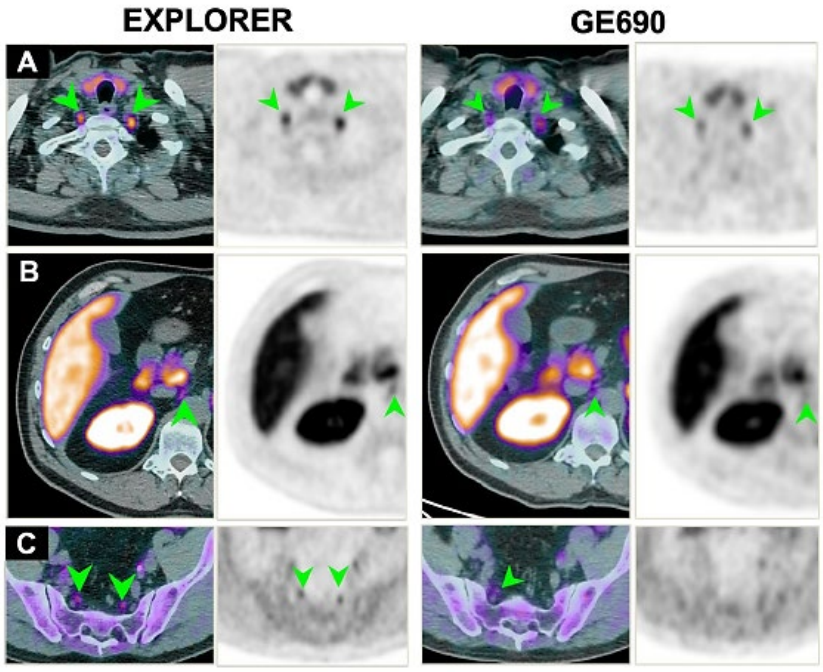

Figure 1. A 59-year-old man with metastatic small bowel neuroendocrine tumor. EXPLORER and GE690 PET/CT images revealed clear visualization of stellate ganglia bilateral (A), while the right celiac ganglia is well-visualized on EXPLORER (B) compared to very faint uptake on conventional scanner (B). The presacral ganglia at S1 are almost only visualized on EXPLORER (C).

Diversifying the Subject Cohorts in Total-Body PET Research: A Feasibility Study

[1,2]Ramsey D Badawi, [3]Alexandra CT Gori, [1,2]Simon R. Cherry, [3]Julie HT Dang, [1]Lynda E. Painting, [1]Benjamin A. Spencer, [4]Doreen Pichotti, [4]Stephanie A. Winn, [1]Lorenzo Nardo, [3]Moon S. Chen, Jr.

[1]Department of Radiology, UC Davis, [2]Department of Biomedical Engineering, UC Davis, [3]Cancer Center, UC Davis, [4]Public Affairs & Marketing, UC Davis

Introduction: Early studies using the EXPLORER total-body PET scanner at UC Davis recruited 30 healthy subjects that for the most part had local knowledge of the technology. This initial population was not representative of the community that UC Davis Health serves. The goal of this feasibility study was to initiate and evaluate an approach to promote greater research cohort diversity, especially of under-represented racial/ethnic groups.

Methods: A pilot study was opened targeting recruitment of 20 healthy subjects from under-represented racial/ethnic groups. In collaboration with the UC Davis Comprehensive Cancer Center's (UCDCCC) Community Advisory Board (CAB), we reviewed existing publicity material and noted that there was little representation of anyone of color. Together, we created additional publicity material. CAB members were invited to take a "ride" on the EXPLORER. CAB members' experiences were video recorded. TV broadcasts (11), radio advertisements (32) and news articles (3), reached thousands of community members in the local area. Publicity photographs produced before and after consultation with the CAB are shown in Figure 1 (top). In this pilot study, the assessed outcome variables were number of subjects inquiring about the study and number of subjects enrolled.

Results: 155 inquiries were received from the public. Twenty subjects were enrolled, meeting the enrollment target for the protocol. Subjects underwent total-body dynamic FDG scans with additional static acquisitions. The self-reported racial and ethnic breakdown of the original study and of the enrolled subjects following the outreach are shown in Figure 1 (bottom).

Discussion and Conclusions: Use of publicity materials and outreach approaches designed in consultation with the Community Advisory Board yielded a diverse subject cohort. This study provides a template for outreach and recruitment efforts for future research studies which aim to be more representative of the diversity of the local community.

Self-Reported Race/Ethnicity	*Pre-outreach cohort*	*Post-outreach cohort*
Asian	1	5
Native American	0	2
Black	0	7
White-hispanic	1	6
White/non-hispanic	15	0
Not reported/declined to state	13	0

Figure 1. (Top) Representative EXPLORER publicity shots; left: prior to consultation with the CAB, right: after consultation with the CAB. (Bottom) Self-reported race and ethnicity distribution for cohorts enrolled before and after outreach.

Validation and Optimization of a Scatter Correction Method for Total-Body Positron Emission Tomography

[1]R. Bayerlein, [2]Z. Xie, [1,2,3]E.K. Leung, [1]Y.G. Abdelhafez, [1,2]B. A. Spencer, [2]N. Omidvari, [2]Q. Wang, [2]E. Li, [1]L. Nardo, [1,2]S. R. Cherry, [1,2]R. D. Badawi

[1]Department of Radiology, UC Davis Health, Sacramento, CA, USA, [2]Department of Biomedical Engineering, University of California Davis, CA, USA, [3]UIH America, Inc., Houston, TX, USA

The uEXPLORER is a 2-m-long total-body PET scanner which provides improved image quality and increased sensitivity compared to conventional scanners. However, due to vastly increased data sizes, image reconstruction and data correction techniques (like scatter correction, SC) become computationally more challenging. We now present a recently developed Monte Carlo-based SC method.

The tool was developed using images reconstructed with 3D-TOF-OSEM with point spread function-modeling, corrections for attenuation, dead-time, and random events, and without image post-processing filters. Simulation-based scatter correction factors were calculated after every OSEM iteration.

The image quality was quantitatively assessed using phantom scans following the NEMA NU 2-2018 protocol. The contrast recovery coefficient in scatter corrected images was up to 18.2 percentage points higher than without SC, and the residual lung error was reduced by about a factor of three.

Furthermore, an 83 y/o patient with lung cancer was scanned for 20 min (120 min p.i., 373.7 MBq [18F]FDG), and reconstructed with the above parameters. The scatter corrected image showed better apparent diagnostic image quality with increased lesion conspicuity, especially in metastases in adrenal glands and lymph nodes.

The average peak-to-valley-ratio (PVR) along a line profile through the center of 13 vertebrae was calculated. The PVR in the scatter corrected image was 3.46 compared to 1.98, without SC.

The scatter removal in the trachea was also quantified: despite residual scatter contamination inside the trachea, the average activity concentration was 31.0% lower than in peripheral lung tissue (6.9% lower without SC).

A SC technique was successfully implemented and quantitatively and qualitatively validated. These results serve as a basis for further optimizing accuracy and performance. We are currently testing different scaling methods and are investigating the minimum number of required SC iterations and number of events and envisage cloud-based computing for performance enhancement.

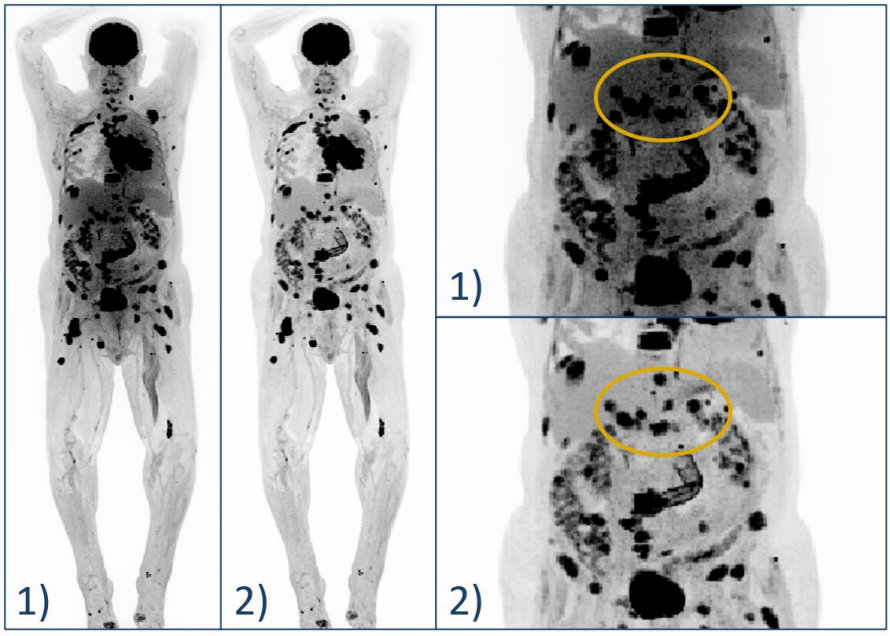

Fig. 1. MIPs of a total-body PET scan of a human subject without SC (#1) and with SC (#2). The orange oval contours the region with the most noticeable changes.

^{18}F-FDG Gallbladder Uptake: Observation from a Total-Body PET/CT Scanner

[1,2]Anna Calabro, [2,3]Yasser G. Abdelhafez, [4]Elizabeth K.A. Triumbari, [2,5]Benjamin A. Spencer, [6]Moon S. Chen, Jr., [1]Domenico Albano, [7]Christopher R. Cassim, [1]Francesco Bertagna, [1]Francesco Dondi, [2,5]Simon R. Cherry, [2,5]Ramsey D. Badawi, [2]Fatma Sen, [2]Lorenzo Nardo

[1]Nuclear Medicine Department, University of Brescia and ASST Spedali Civili di Brescia, Brescia, Italy, [2]Department of Radiology, [3]Nuclear Medicine Unit, South Egypt Cancer Institute, Assiut University, Egypt, [4]Nuclear Medicine Unit, TracerGLab, Fondazione Policlinico Universitario A. Gemelli IRCCS, Rome, Italy, [5]Biomedical Engineering, and [6]Internal Medicine, University of California Davis, Davis, CA, USA, [7]Department of Radiology, Sangre Grande Hospital, Eastern Regional Health Authority, Sangre Grande, Trinidad & Tobago

INTRODUCTION: Long axial field of view PET/CT scanners are characterized by higher signal collection efficiency and greater spatial resolution. The gallbladder is not usually visualized as an ^{18}F-FDG-avid structure in routine clinical PET/CT studies, unless affected by an infective, inflammatory, or neoplastic process. In this study we report visualization rates and characteristics of gallbladder ^{18}F-FDG uptake observed in both healthy and oncologic subjects on EXPLORER PET/CT system.

METHODS: Scans from 73 participants (48 healthy and 25 with newly diagnosed lymphoma) who underwent ^{18}F-FDG total-body PET/CT were retrospectively reviewed. Subjects were scanned at multiple timepoints up to 12 hours post-injection. High-fat high-protein meal was provided after the 180-minute timepoint. Gallbladder ^{18}F-FDG uptake was graded using liver uptake as a reference, and the pattern was qualified as present in the wall, lumen, or both. Participants' characteristics were collected to assess for any significant correlation with gallbladder ^{18}F-FDG uptake. CT images were visually assessed for presence of gallbladder stones and biliary sludge.

RESULTS: The detection rate for gallbladder ^{18}F-FDG uptake was 100% at 120- and 180-minute post-injection scans. No uptake was observed after the 180-minute scan in 15 participants imaged up to 12 hours. All 73 subjects showed gallbladder uptake at one or more imaging timepoints. An increase in uptake intensity overtime was observed up until the 180-minute scan, and gallbladder wall uptake was observed at early timepoints whereas luminal activity was the prevalent pattern at delayed timepoints. No significant correlation was found between gallbladder uptake intensity/pattern and subjects' characteristics.

DISCUSSION: The consistent observation of gallbladder ^{18}F-FDG uptake recorded in this study in healthy participants and oncologic subjects was detectable because of the properties of new generation total-body PET/CT scanners.

CONCLUSION: Gallbladder visualization on ^{18}F-FDG total-body PET/CT scans is likely a normal physiologic process and should not be mistaken for any pathology.

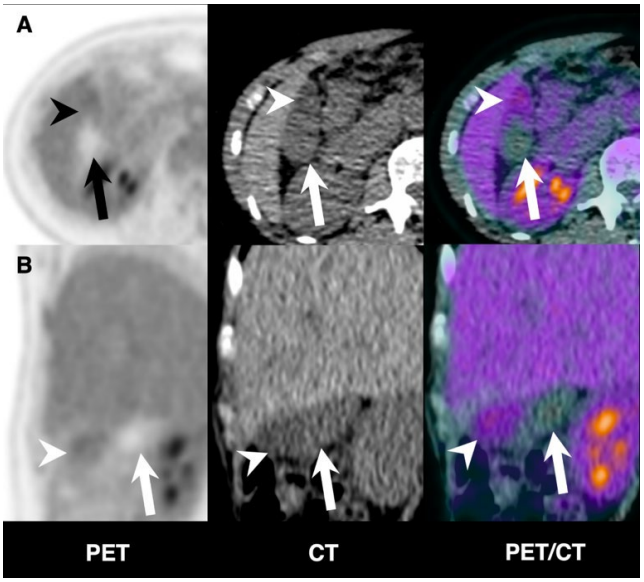

Axial (A) and sagittal (B) PET, CT and fused PET/CT images of a 61 y/o healthy female participant, scanned at 90-minute post-injection of 334 MBq of 18F-FDG. Images show distribution of ^{18}F-FDG uptake in the gallbladder: one portion shows uptake with lower attenuation on the corresponding CT (arrowhead), while the other portion shows no uptake and higher attenuation on the corresponding CT (arrow). These findings suggest the presence of different luminal content, suggestive of biliary sludge.

Using total body PET to elucidate whole-body metabolism in the tissue-specific level

[1,2]Maria Chondronikola, [2]Yasser G. Abdelhafez, [2]Abhijit J Chaudari, [2]Gubao Wang, [2,3]Simon R. Cherry, [2,3]Ramsey D. Badawi

[1]Nutrition, Nutrition, Washington Univ SOM, St. Louis, [2]Department of Radiology, UC Davis, [3]Department of Biomedical Engineering, UC Davis

Introduction: Perturbations of energy homeostasis (such as obesity and cachexia) are global public health issues worldwide as they affect the health and quality of life of the population. Understanding the pathophysiology of this systemic diseases is of critical importance for the development of future therapeutic interventions to improve clinical outcomes. The multi-organ nature of the pathophysiology of obesity and cachexia presents a unique challenge. Total body positron emission tomography (PET) imaging provides an important tool to understand multi-organ metabolic function in the whole-body level with tissue-specific resolution and to study organ crosstalk.

Planned Collaboration: To this end, faculty from the UC Davis Departments of Radiology and Nutrition have agreed to develop, test, and apply total body PET imaging in conjunction with ^{18}F-fluorodeoxyglucose (^{18}F-FDG) administration to assess glucose kinetics in the whole-body level with tissue-specific resolution in participants with metabolically unhealthy obesity, patients with cancer cachexia, and healthy individuals. The steps involved in establishing the final workflow are the following: i) 60-min dynamic PET after intravenous ^{18}F-FDG administration followed by a low-dose computed tomography (CT); ii) automated organ segmentation using existing software applications, iii) parametric analysis of the PET imaging data and calculation of kinetic parameters in each tissue, and iv) network analysis to elucidate organ crosstalk.

Impact: Developing and establishing the methods needed for the visualization and quantification of whole-body metabolic function with tissue-specific resolution using total body PET will provide essential information to better understand disease physiology and potentially develop diagnostic and therapeutic modalities.

Quantitative T_2 mapping as a biomarker of neuropathology resulting from acute organophosphate intoxication in a rat model

[1,2]Alita Jesal D'Almeida, [3]Brad A. Hobson, [1,2]Valerie A. Porter [5]Joel R. Garbow, [4]Pamela J. Lein, [2,3]Abhijit J. Chaudhari

[1]Biomedical Engineering; [2]Radiology; [3]Center for Molecular and Genomic Imaging; [4]Molecular Biosciences, University of California, Davis; [5]Radiology, Washington University St Louis, Missouri

Introduction: Acute intoxication with organophosphates (OPs) present in nerve agents and pesticides causes life threatening cholinergic crisis, seizures, and long-term neurologic consequences. T_2 relaxation time (T_2-mapping) from MRI has been used to assess the spatiotemporal progression of these pathologies. However, little data exists to characterize these pathologies beyond the first few days of OP intoxication. The objective of this study was to assess T_2 mapping as a biomarker for characterizing long-term neuronal consequences of OP intoxication and neuroprotective therapies in a rodent model.

Methods: Adult Sprague Dawley rats were imaged at days 3, 7 and 28 post-intoxication with the OP diisopropylfluorophosphate, (DFP, n=32, VEH, n=13) using a spin-echo pulse sequence with 15 echo times (TEs). Three therapies were investigated: midazolam (MDZ, n=29), a neurosteroid allopregnanolone (ALO, n=28), a combination (DUO, n=28). The hippocampus (H) and piriform cortex (PC) were manually delineated given their known significance as targets of OPI. A mono-exponential curve fit was performed with MATLAB using 2 approaches: (1) Voxel-wise quantification: curve fitting the intensity-TE curves for each voxel, providing a voxel-wise map of T_2 values; and (2) Regional quantification: regionally averaging the intensity curves at each TE, performing one curve fit and obtaining a single T_2 value per region.

Results and Conclusion: For both modeling approaches, the DFP group had longest T_2 values compared to treatment groups ($p<0.05$). VEH T_2 values were within the range reported in the literature. T_2 values of OP-intoxicated rats were longest on day 3 and decreased with time. The voxel-wise quantification method showed a larger variation in T_2 values within regions, suggestive of intra-regional heterogeneity of neuronal damage consistent with visible lesions on T_2-weighted images (Figure 1). This study demonstrates the potential of T_2 mapping as a quantifiable biomarker to longitudinally track neuropathology post OP intoxication.

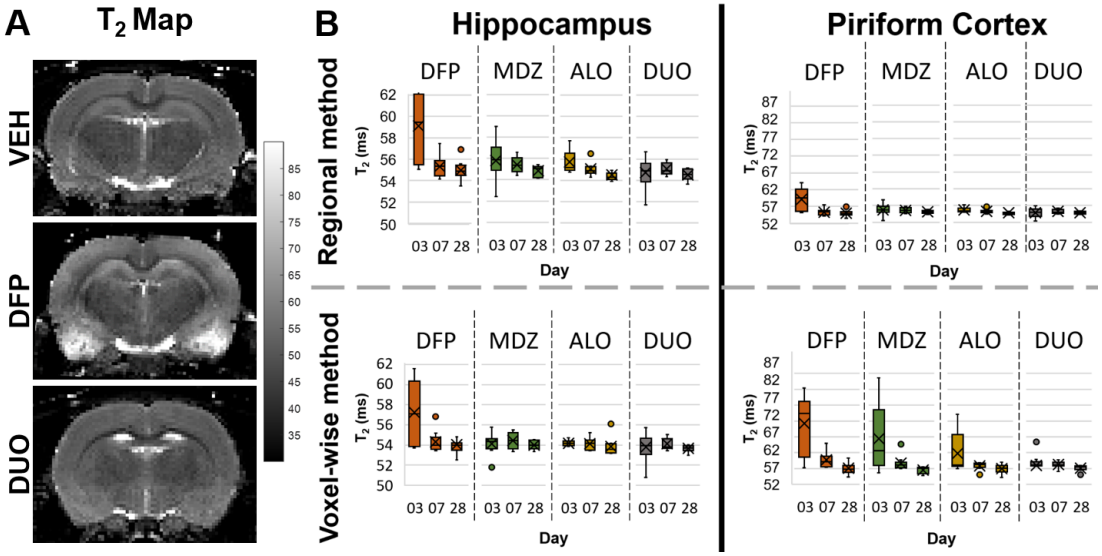

Figure 1) (A) T_2 maps on Day 3 of VEH, DFP, and DUO groups. Color bar shows T_2 values in ms; (B)T_2 value distribution for hippocampus and piriform cortex across groups and with voxel-based (top row) and regional (bottom row) quantification methods.

A Monte Carlo analysis of Guidewire Safety Comparing a Body and Local coil

[1]Felipe Godinez, [2]Jeff Hand, [2]Nuno J Treixeira, [3]Bart R Steensma, [2]Joseph V Hajnal, [4]Alexander J. E. Raaijmakers, [2]Shaihan J Malik

[1]Department of Radiology, University of California Davis, Sacramento, California, USA
[2]School of Biomedical Engineering and Imaging Sciences, King's College London, London, UK
[3]Center for Image Sciences, Computational Imaging Group, University Medical Center Utrecht, Utrecht, Netherlands, [4]Biomedical Engineering, Medical Imaging Analysis, Eindhoven University of Technology, Eindhoven, Netherlands

Introduction: In MRI, Interventional devices are unsafe due to heating caused by coupling to the transmit coils of the scanner. A novel solution is to design a transmit coil with a small electric field footprint, in comparison to a body coil which emits a larger electric field. Using simulation, the potential for heating at the device tip was evaluated by comparing a local coil array and a body coil.

Methods: The electric transfer function for a 100cm long wire in a dielectric medium (insertion depths: 100cm, 80cm, 70cm, 60cm, 40cm) was calculated from simulated excitations with a plane wave at the tip. The guidewire was modeled as an insulated 1mm wire with 5mm of the tip exposed by removing the insulation. A full human sized phantom was excited with a local coil array with 8 coil loops, with 4 coils posterior and 4 anterior, and a body coil (bird cage coil) 45cm long with 16 rungs, for comparison. Ten thousand wire trajectories were randomly generated in the phantom. The scattered electric field at the tip was computed by integrating the tangential component of the electric field produced by either coil along each wire trajectory multiplied by the relevant wire electric transfer function.

Results: The body coil to local coil array ratios for the mean electric power at the tip were 1.7, 1.9, 2.4, 2.7, 2.5, and 2.3 for depths 100cm to 40cm, respectively. The 99th percentile electric power at the tip (close to worst case) was 98%, 40%, 115%, 198%, 175%, and 125% greater for the body coil, for depths 100cm to 40cm, respectively.

Conclusion: We have compared a body coil with a local transmit coil and numerically evaluated the heating risks that each can pose on many different guidewire trajectories in a dielectric medium. In most cases the local coil array was the safer coil.

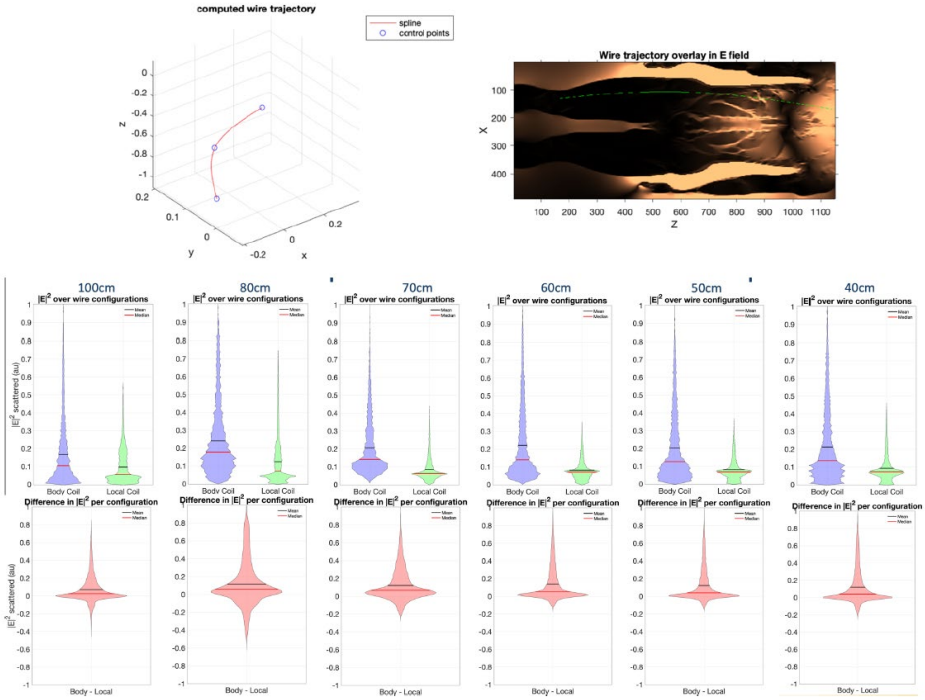

The calculated spline trajectory in MatLab (top left). The overlay of the projection of the tangential component along the guidewire and the incident electric field is shown (top right). The Violin plots of the electric power at the wire tip for each wire trajectory/geometry for the body coil and local coil, respectively (middle row). Violin plots of the difference in electric power between the body coil and local coil (bottom row).

Non-invasive quantification and SUVR validation of [^{18}F]-florbetaben with total-body EXPLORER PET

[1]Emily N. Holy, [1]Charles DeCarli, [1]Evelyn Rebekha Alfaro, [1]Evan Fletcher, [1]Anjan Bhattarai*, [2,3]Benjamin A. Spencer, [2,3]Simon R. Cherry, [3]Audrey P. Fan
*will be presenting

[1]Department of Neurology, UC Davis, [2]Department of Radiology, UC Davis, [3]Department of Biomedical Engineering, UC Davis

Introduction: The total-body EXPLORER PET scanner supports the acquisition of a full human body in one scan and permits noninvasive Image-Derived Input Functions (IDIFs) as an alternative to arterial blood sampling (Badawi, JNM 2019). Our aim is to quantify amyloid buildup in older individuals with kinetic models that leverage dynamics in aorta IDIFs and the brain utilizing [^{18}F]-Florbetaben EXPLORER PET and validate with standardized uptake value (SUVR).

Methods: Fourteen adults (9 cognitively-normal, 2 Mild Cognitive Impairment, and 3 Alzheimer's disease) aged 66-86 underwent dynamic total-body ^{18}F-florbetaben PET (United Imaging) for 110min. Regions of interests were drawn in the middle descending aorta and eroded to exclude the vessel walls to derive IDIFs. The PET volumes were motion corrected (FSL-MCFLIRT) and linearly registered (FSL-FLIRT) to T1W image. The DKT ATLAS was used to segment brain cortical regions that are involved in neurodegeneration for PET SUVR measurements. PET SUVR means were calculated from 7 index regions and the cerebellar gray matter as the reference. Dynamic time activity curves from the same brain regions were fit to the two-tissue compartment model (2TCM) using population metabolite-corrected IDIFs; and the Multi-linear Reference Tissue Model (MRTM) to calculate distribution volume ratio (DVR) with reference to cerebellar gray (Ichise, JCBFM 2003).

Results: Amyloid-positive patients showed the highest SUVR in brain index regions individually. Higher SUVR accumulation was observed in index regions compared to cerebellum at later time points in amyloid-positive cases. SUVR and DVR from kinetic models were strongly correlated; with slight overestimation of SUVR compared to DVR. DVR values from the MRTM were lower than (86.7% of) DVR quantified by 2TCM.

Discussion: Absolute quantification of amyloid binding from total-body [^{18}F]-florbetaben PET data is feasible using aorta IDIFs and shows high agreement to SUVR in discriminating positive and negative scans.

Conclusions: Total-body EXPLORER PET enables high quality kinetic modeling for accurate measures of amyloid accumulation in clinical research of aging and dementia.

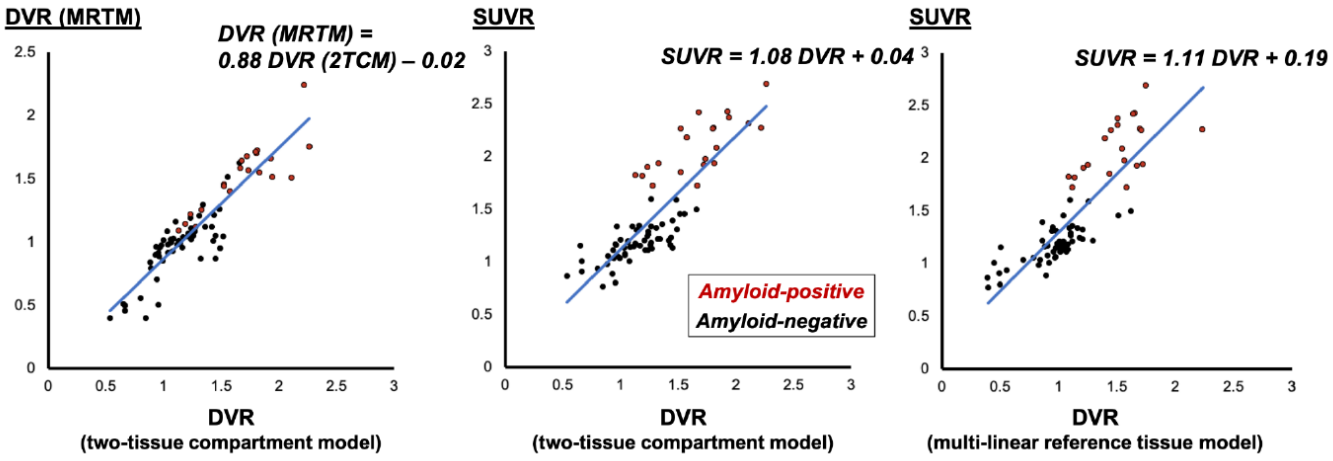

Figure 1. Linear regression analysis of amyloid quantification in brain index regions with correction for subject clustering.

Pediatric Intranodal CT Lymphangiography with Water-Soluble Contrast Media

[1]Zachary B. Jenner, [1]Peter Li, [1]Brian W. Goldner, [1]Ahmadreza Ghasemiesfe, [1]Ryan T. Di Geronimo, [1]Colin N. Brown, [1]Gary W. Raff, [1]John Kaufman, [1]Lisa Kang

[1]Department of Radiology, UC Davis

Purpose: To describe a novel lymphatic imaging technique: pediatric ultra-high resolution CT lymphangiography (UHR CTL) with water-soluble iodinated contrast via direct inguinal intranodal injection. UHR CTL is particularly beneficial in complex congenital heart disease patients with postoperative high-mortality continuous chylothorax and right-to-left shunt.1

Materials & Methods: *Intranodal injection.* US-guided direct inguinal intranodal injection was performed as previously described.2,3 Under fluoroscopic guidance, intermittent pulsed intra-nodal iodinated contrast injection (3.2 mL total, ~1 mL/kg body weight) continued until contrast was visualized in the upper abdominal lymphatics. Limited intermittent CT fluoroscopy confirmed contrast propagation to the upper mediastinum and lower neck.

UHR CTL technique. Non-contrast and intra-lymphatic contrast enhanced UHR CT images of the chest, abdomen, and pelvis were helically acquired with a 160 row x 0.25 mm detector element and thickness 0.25 mm, tube voltage 80-100 kVp, and iterative reconstruction. Immobility is vital to diagnostic quality; ICU managed intubation and sedation during image acquisition.

Results: Water-soluble pediatric UHR CTL was successfully performed without complication. US-guided intra-nodal injection rapidly opacified the central lymphatic system. Intermittent fluoroscopy identified contrast progression along the abdominopelvic lymphatics, but was unable to delineate the thoracic duct. With UHR CTL, the thoracic duct and lymphovenous junction were visualized 10-15 minutes after injection, lymphatic leakage site(s) were identified, and the thoracic duct was void of contrast 30 minutes after injection. A typical case can be performed in 2 hours of room time. In infants, fluoroscopy was performed with 1-2 minutes of fluoro time (~ 1 mGy), and base, CT fluoroscopy, and CTL scans were performed with low radiation dose (CTDIvol 10-15 mGy and total DLP 100-200 mGy).

Conclusion : To the best of our knowledge, this is the first technical description of water-soluble pediatric UHR CTL. Water-soluble iodinated contrast offers superior diagnostic quality compared to lipiodol, is safe in patients with right-to-left shunting, and rapidly identifies the central lymphatic drainage pathways. CTL is a viable alternative to MR lymphangiography and likely provides superior spatial resolution in infants and small children. The procedures were safe and accurately delineated small lymphatic structures, which is a vital diagnostic capability for patients with high-mortality continuous chylothorax.

References

1. A. Burgin CB, N. Kolicaj, S. Schwartz;. Review of techniques for percutaneous lymphangiography and thoracic duct cannulation for treatment of chylothorax. Abstract Only. *J Vasc Interv Radiol*. 02/01/2015 2014;26(2):S169. doi: https://doi.org/10.1016/j.jvir.2014.12.453

2. Chavhan GB, Amaral JG, Temple M, Itkin M. MR Lymphangiography in Children: Technique and Potential Applications. *Radiographics*. Oct 2017;37(6):1775-1790. doi:10.1148/rg.2017170014

3. Nadolski GJ, Itkin M. Feasibility of ultrasound-guided intranodal lymphangiogram for thoracic duct embolization. *J Vasc Interv Radiol*. May 2012;23(5):613-6. doi:10.1016/j.jvir.2012.01.078

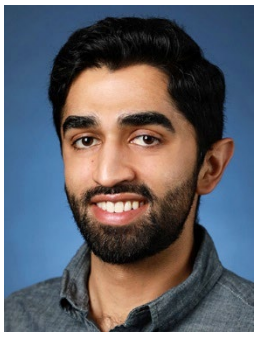

The Effect of Co-Axial Incisions on the Traction Removal Force of Mushroom-Retained Gastrostomy Tubes

Abdullah Khan

Department of Radiology, UC Davis

Introduction: Removal of mushroom-retained tubes is associated with trauma along the stoma tract producing pain, bleeding, and site infection. We aim to provide proof-of-concept data for an alternative removal technique by evaluating the effect of co-axial incisions of the mushroom-retention gastrostomy tube on the required force for removal.

Methods: An ex-vivo model of the and gastrostomy stoma was fabricated with a polyethylene through which a mushroom-retained gastrostomy tubes may be introduced. Three tube sample groups were created representing unmodified 20 Fr tubes, and 20 Fr tubes with one, or two co-axial cuts extending though the mushroom retention feature. The maximum force required for tube removal via traction was measured with a digital force sensor. The required forces for each sample group were compared using a two sample t-test.

Results: A total of 70 traction removal procedures of mushroom-retained gastrostomy tubes were conducted. In comparison to an unmodified tube, reduction in the mean force required for removal was statistically significant in both the single axial cut group ($p < 0.05$) and the two co-axial cut group ($p \ll 0.05$). The addition of co-axial incisions facilitated the folding of the mushroom-retention mechanism and reduced the amount of deformation required to fold through the tract.

Discussion: Axial incisions of a mushroom-retained gastrostomy tube result in statistically significant reduction in the traction force required for removal in our benchtop model. The current study supports the development of an instrument that may safely and efficaciously create co-axial incisions in an in-situ mushroom-retained gastrostomy tube.

Conclusion: An instrument that creates axial incisions of a mushroom-retained gastrostomy tube would result in a decrease in the required force for removal and theoretically decreased trauma to the stoma tract.

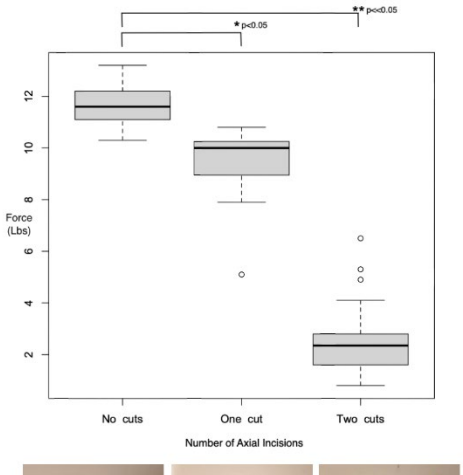

Figure 1a. Box plot representation of the force of gastrostomy tube removal in the three tube groups. Reduction in the mean force required for removal was statistically significant in both axial cut groups.

Figure 1b. Images depicting gastrostomy tube mushroom retention discs with no incisions, one axial incision, and two axial incisions.

Lesion Detectability in Contrast-Enhanced Breast CT using Model Observers

[1]Su Hyun Lyu, [1]Andrew M. Hernandez, [2]Craig K. Abbey, [1]John M. Boone

[1]Department of Radiology, UC Davis, [2]University of California, Santa Barbara

Introduction: Imaging protocols in contrast-enhanced breast CT (bCT) should be optimized for lesion detection and is dependent on a host of factors. In this study, we quantitatively evaluate the improvement in lesion detectability due to contrast enhancement across lesion diameter, section thickness, and breast density using a pre-whitened matched filter (PWMF) model observer.

Methods: The relationship between iodine concentration and HU was measured using a rod phantom containing known iodine concentrations placed in a polyethylene breast phantom and scanned on a prototype bCT system. Mathematically generated spherical mass lesions of varying diameters and contrast enhancement levels were inserted at random locations in 139 actual patient bCT datasets. Images with varying section thicknesses were generated by slice averaging. The volumetric glandular fraction (VGF) of the patient datasets was quantified using a previously reported algorithm. A PWMF was generated for combinations of lesion diameter, contrast enhancement, section thickness, and breast density. The PWMF detection performance was assessed using the area under the ROC curve for 200 lesions and non-lesions per breast and parameter combination.

Results and Discussion: In unenhanced bCT, optimal display section thickness is at 75% of the lesion diameter. When section thickness is less than 4mm, contrast enhancement enables detection of lesions greater than 1mm in diameter 100% of the time. In unenhanced bCT, a monotonic decrease in detection performance is observed as breast density increases across all lesion sizes. In contrast-enhanced bCT, detection performance is minimally dependent on breast density across all lesion sizes.

Conclusion: This study demonstrates quantitatively how lesion detectability improves with contrast enhancement in bCT across relevant parameters. Contrast imaging protocols can be optimized depending on patient breast density and estimated size of lesion being detected.

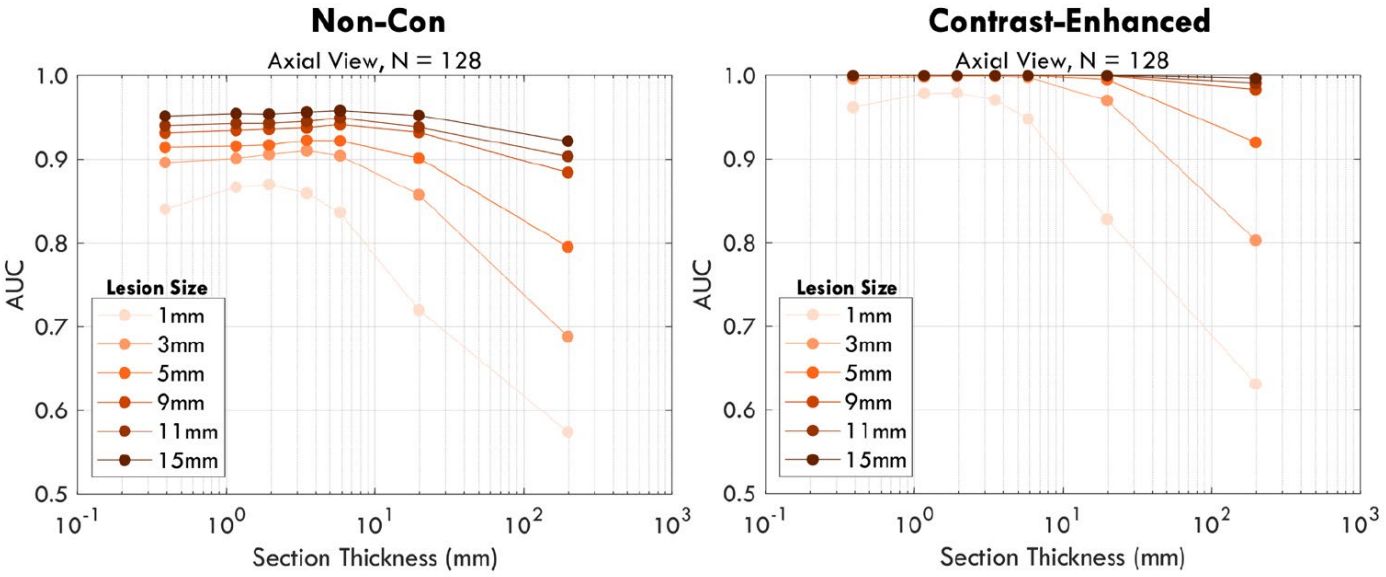

Figure caption: Left) Effect of section thickness in unenhanced bCT for lesion sizes 1, 3, 5, 9, 11, 15 mm. Right) Effect of section thickness in contrast-enhanced bCT for lesion sizes 1, 3, 5, 9, 11, 15 mm.

Utilization of EOS™ Imaging for Evaluation of Bowel Management and Radiation Dose Reduction

[1]Kriti Gwal, [1]Rebecca Stein-Wexler, [2]Shinjiro Hirose, [2]Payam Saadai

[1] Department of Radiology, UC Davis, [2]Department of Surgery, UC Davis

Introduction: This study assesses the impact on radiation dose of EOS™ imaging system (EOS) versus computed or digital radiography (CR/DR) to assess fecal burden on abdominal radiographs in children undergoing bowel management programs.

Methods and Materials: We retrospectively identified 39 patients in Shriner's Bowel Management Program being treated for chronic constipation who had abdominal radiographs obtained with EOS and CR/DR between 07/01/2017-05/30/2018. We compared dose area product (DAP) for EOS radiographs with DAP for CR/DR radiographs on the same patients. Dose comparison was performed with calculation of difference, percent dose reduction, and paired t test.

Results: Percent reduction in DAP ranged from 17.9% to 94.5%. Mean dose with EOS showed an overall decrease of 82% when compared to mean CR/DR DAP (p=0.005).

Discussion: There is a constant drive for radiation dose reduction in children. The Image Gently campaign and ALARA principle promote using the lowest possible radiation dose, while obtaining diagnostic imaging. EOS allows for especially low radiation dose by being sensitive to photons and reducing scatter radiation. It utilizes slot scanning to image upright patients, acquiring AP and lateral images simultaneously, in two and/or three dimensions. EOS is usually used for orthopedic purposes, specifically bone alignment.

We found that EOS' ability to decrease radiation dose while maintaining image quality has another application. It is useful for children enrolled in bowel management programs. These children undergo multiple clean-out regimens and other bowel hygiene programs and require serial radiographs to evaluate stool burden. EOS makes it possible to evaluate trends in stool burden—and treatment efficacy—using lower radiation dose than CR/DR, without losing important diagnostic information.

Conclusion: An abdominal radiograph with short exposure time performed by EOS may decrease DAP compared to DR/CR in children in bowel management programs who have serial radiographs to evaluate stool burden.

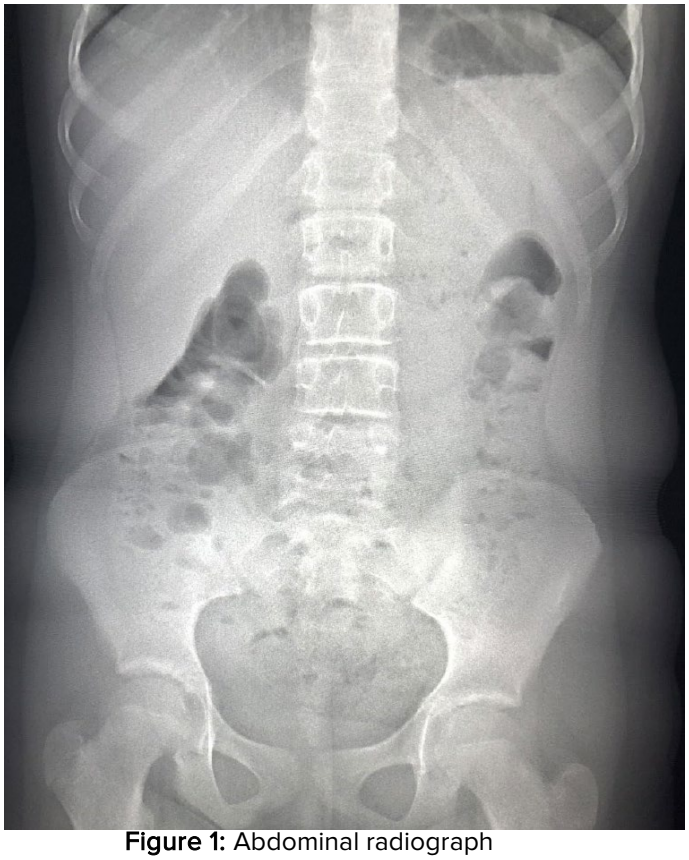

Figure 1: Abdominal radiograph clearly depicts moderate stool burden

Interstitial Space Properties of ^{18}F-fluorodeoxyglucose in Nonalcoholic Fatty Liver Disease

[1]Quyen Tran, [2]Karen E. Matsukuma, [1,4]Benjamin A. Spencer, [1]Yiran Wang, [4]Elizabeth Li, [1]Michael T Corwin, [1,4]Simon R. Cherry, [1,4]Ramsey D. Badawi, [1,5,6]Souvik Sarkar, [1]Guobao Wang

[1]Department of Radiology, UC Davis, [2]Department of Pathology and Laboratory Medicine, UC Davis, [3]Department of Internal Medicine, UC Davis, [4]Department of Biomedical Engineering, UC Davis, [5]Department of Internal Medicine, UC Davis, [6]Florida Research Institute

Objective: Interstitial space is the fluid space surrounding tissue cells. Transport and uptake properties of the radiotracer ^{18}F-fluorodeoxyglucose (FDG) in this space may be distinct in health and disease. Conventional dynamic PET imaging cannot decode this space due to the limited temporal resolution (10-20s/frame). Here we demonstrate the use of high-temporal resolution (2s/frame) dynamic imaging and advanced tracer kinetic modeling enabled on the EXPLORER total-body PET system to explicitly characterize the hepatic interstitial space in nonalcoholic fatty liver disease (NAFLD) and healthy subjects.

Method: Fourteen healthy subjects and ten NAFLD patients were included in this study. Both conventional two-tissue (2T) model, which combines the interstitial space and intracellular space into a free-state space compartment, and the proposed three-tissue (3T) model, which separately models the interstitial space, are used to fit liver time activity curves (TACs). To account for the dual blood supply in the liver, an optimization-derived dual-blood input function (DBIF) approach was utilized. Fitting quality of the 2T-DBIF and 3T-DBIF models was compared by the Akaike information criteria (AIC). The kinetic parameter $K_{1,i}$ (rate of FDG transport from plasma to the interstitial space) and V_i (distribution volume of FDG in the interstitial space) were evaluated for detecting nonalcoholic steatohepatitis (NASH), a more severe form of NAFLD that is determined in NAFLD by biopsy using the total NALFD activity score (NAS) greater than 4.

Result: The 3T-DBIF model provided a better fit quality than the conventional 2T-DIBF model (Fig. 1A), as further demonstrated by the negative AIC difference between the two models in both healthy subjects and NAFLD patients (Fig. 1B). The parameter $K_{1,i}$ (Fig. 1C) and V_i (Fig. 1D) differentiated NASH (NAS > 4) from non-NASH subjects (NAFLD with NAS ≤ 4 and healthy subjects).

Conclusion: This study indicates that FDG characterization of the interstitial space has the strong potential to derive multiparametric PET imaging biomarkers to assess NASH in NAFLD.

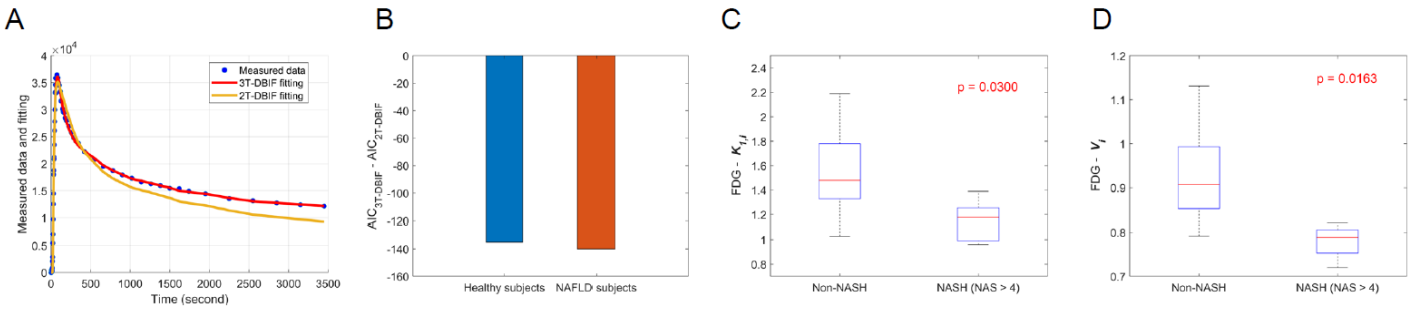

Figure 1. Comparison of 2T-DBIF and 3T-DBIF for fitting liver TACs in NAFLD patients (A). Mean of AIC differences of the two models for all healthy and NAFLD subjects (B). (C-D) NASH subjects (NAS > 4) were associated with lower FDG $K_{1,i}$ (C) and lower V_i (D).

Management of Incidental Findings At The EXPLORER Molecular Imaging Center

[1]Ofilio Vigil, [1]Lorenzo Nardo, [2]John Tupin, [1]Denise Caudle, [1]Cameron Foster, [1.3]Simon Cherry, [1,3]Ramsey Badawi, [1]Dana Little

[1]Department of Radiology, UC Davis, [2]Institutional Review Board, UC Davis, [3]Department of Biomedical Engineering, UC Davis

Introduction: The world's first total-body PET scanner, EXPLORER, is operating at UC Davis Health (UCDH). It is utilized for research purposes and routine clinical PET/CT scanning. Given EXPLORER's long axial field-of-view (194 cm) and ultrahigh physical sensitivity, allowing for simultaneous imaging of the entire body, the discovery of incidental findings (IFs) related to clinical problems in research volunteers is likely, potentially requiring follow-up procedures exposing research participants to additional risks.

Methods: Lacking clear guidance in the context of this first-in-the-world scanner, we developed a plan to address IFs. We relay to participants, via the informed consent form (ICF), the possibility that findings related to a medical problem may be discovered. When an IF is identified, our clinical research team works with the Study Radiologist to contact participants within 8 weeks of the scan to discuss it. However, if the IF requires urgent action, participants are contacted according to the UCDH Department of Radiology guidelines related to emergency findings. During consent, we ask all participants to provide contact information for their medical provider. If a participant requests, we provide them with a subset of their images to share with their medical provider. The research team will send a letter (see Fig 1) to their provider stating the purpose for the scan, the discovery of a potential problem, and the contact information for the Principal Investigator/Study Radiologist.

Conclusion: The method for dealing with IFs is described in all EXPLORER protocols with appropriate language included in the ICF. Our goal is to mitigate risks due to unnecessary follow-up while capturing benefits from important clinical findings obtained during cutting-edge research on EXPLORER.

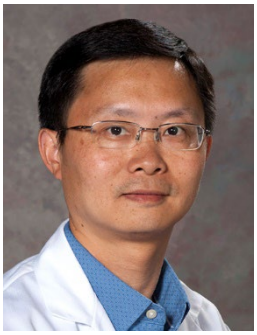

Open Kinetic Modeling Initiatives to Accelerate Quantitative Molecular Imaging Research at UC Davis and in the International Community

[1]Guobao Wang, [1,2]Ramsey D. Badawi, [1]Abhijit Chaudhari, [3]Allison L. Zwingenberger, [1]Lorenzo Nardo, [1]Youngkyoo Jung, [2]Jinyi Qi, [1,2]Simon R. Cherry

[1]Department of Radiology, [2]Department of Biomedical Engineering, [3]School of Veterinary Medicine, UC Davis

Abstract: Radiotracer kinetic modeling is a technique that exploits mathematical models to enable quantitative characterization of targeted physiologically significant molecular process. The technique has a long research history in molecular imaging with positron emission tomography (PET), but its broad clinical applications have been hampered due to limited scanner performance. Along with the recent boost in sensitivity of commercial PET scanners and the advent of total-body PET technology, there is an urgent need to accelerate kinetic modeling research and clinical translation, e.g., for molecular imaging of cancer. However, the field is challenged by insufficient state-of-the-art kinetic modeling resources, limited access to educational opportunities, and a lack of young-generation researchers. We address these challenges by creating a Kinetic Modeling Service (KMS) at UC Davis and by launching an international Open Kinetic Modeling Initiative (OpenKMI). The KMS offers advanced kinetic modeling methods as a service to clinical and preclinical investigators. The service is becoming available via the UC Davis EXPLORER Molecular Imaging Center for human studies, the Center for Molecular and Genomic Imaging for small animal and non-human primate studies, and the Companion Animal Imaging Center for large animal studies. The OpenKMI for the international community is being created in collaboration with leaders from multiple institutions (e.g., Yale University, UCSF) and with initial grant support from the IEEE Nuclear and Plasma Sciences Society. The initiative includes an educational effort to organize open-access short courses and webinars on specific technical topics, and a resource effort that opens datasets and codes to promote the development and broad dissemination of tracer kinetic modeling to the wider technical society. The two internal and external initiatives are expected to help accelerate quantitative molecular imaging research and translation both at UC Davis and across international sites.

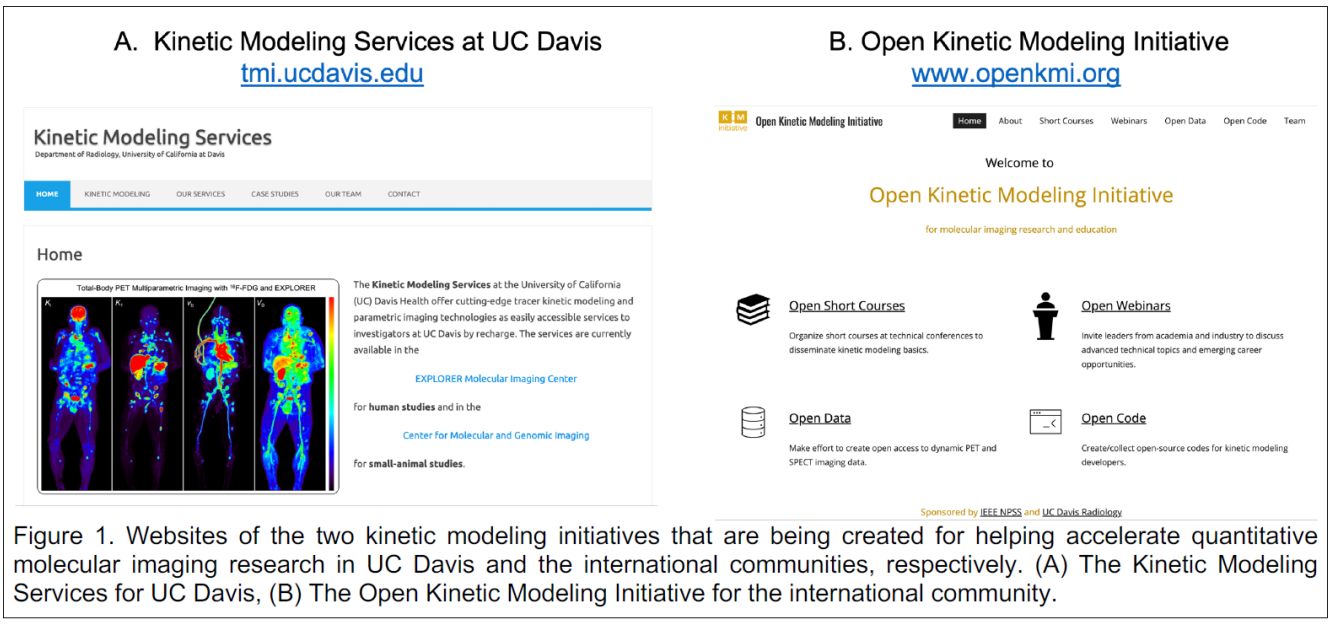

Figure 1. Websites of the two kinetic modeling initiatives that are being created for helping accelerate quantitative molecular imaging research in UC Davis and the international communities, respectively. (A) The Kinetic Modeling Services for UC Davis, (B) The Open Kinetic Modeling Initiative for the international community.

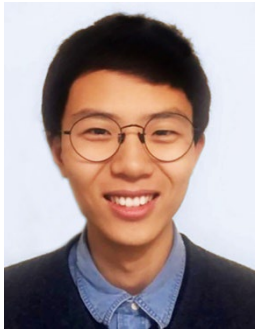

Multi-organ metabolic changes in COVID-19 recovery measured with total-body dynamic ^{18}F-FDG PET

[1,2]Yiran Wang, [1]Lorenzo Nardo, [1,2]Benjamin A. Spencer, [1]Yasser G. Abdelhafez, [1]Abhijit J. Chaudhari , [1,2]Ramsey D. Badawi, [1,2]Simon R. Cherry, [1]Guobao Wang

[1]Department of Radiology, [2]Department of Biomedical Engineering, UC Davis

Introduction: COVID-19 can affect multiple organs and the prolonged impacts have not been thoroughly investigated. Total-body dynamic ^{18}F-FDG PET, e.g., on the 2-m long uEXPLORER system, combined with kinetic modeling permits a quantitative evaluation of metabolism in the entire body. In this paper, we investigate the metabolic changes in multiple organs of COVID-19 subjects in the early recovery period using total-body dynamic ^{18}F-FDG PET and kinetic modeling.

Methods: The study enrolled thirteen healthy subjects and eight recovering COVID-19 patients who were within two months of confirmed diagnosis. Each subject had an ^{18}F-FDG scan on the uEXPLORER system for one hour. Regions of interest (ROIs) were placed in multiple organs in the reconstructed total-body images to obtain parameters. The ROI-based parameters include the standardized uptake value (SUV), SUV ratio relative to blood (SUVR), ^{18}F-FDG rate constants K_1~k_4 by compartmental modeling, and net influx rate $K_i = K_1 k_3 / (k_2 + k_3)$. T-tests were performed to examine differences between the two groups over the parameters. We further generated parametric images to confirm the ROI-based analysis.

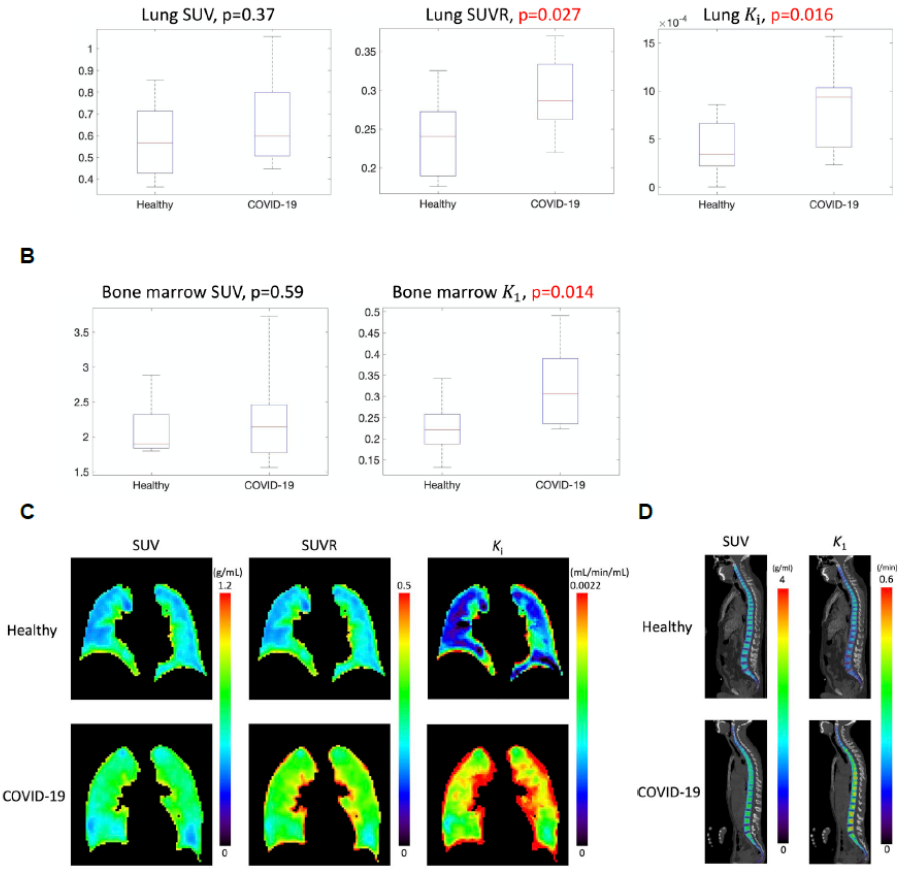

Discussion: The increases in ^{18}F-FDG lung metabolism (represented by SUVR and K_1) and bone marrow ^{18}F-FDG delivery may imply prolonged inflammation and immune response during the early recovery.

Conclusion: We detected increased lung glucose metabolism and bone marrow glucose delivery of recovering COVID-19 patients, which suggests continued impacts in early recovery. Kinetic quantification enabled by total-body dynamic ^{18}F-FDG PET provides a sensitive tool to monitor the metabolic changes in multiple organs.

Figure 1. A. Comparison of SUV, SUVR and ^{18}F-FDG net influx rate K_i between the healthy and the recovering COVID-19 groups. **B**. Comparison of SUV and ^{18}F-FDG delivery rate K_1 between the two groups. **C**. Lung SUV, SUVR and K_i parametric images of one example healthy subject and one example recovering COVID-19 subject. **D.** Bone marrow SUV and K_1 parametric images of the two subjects.

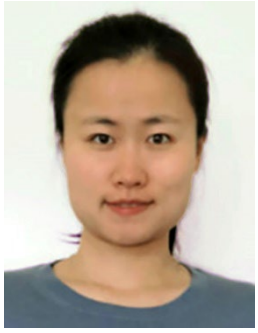

Cross-validation log-likelihood regularization strength optimization in penalized likelihood reconstructions for total-body and conventional PET

[1,2]Qian Wang, [1]Xuezhu Zhang, [1]Zhaoheng Xie, [1,2]Benjamin A. Spencer, [2]Reimund Bayerlein, [1,2,3]Edwin K. Leung, [2]Yasser G. Abdelhafez, [1]Jinyi Qi, [1,2]Simon R. Cherry, [1]Lorenzo Nardo, [1,2]Ramsey D. Badawi

[1]Department of Radiology, [2]Department of Biomedical Engineering, [3]UIH America, Inc., Houston, TX, USA

Introduction: The penalized likelihood (PL) reconstruction is a widely used PET image reconstruction algorithm particularly effective for low count-density data. However, its regularization strength is typically chosen empirically. To select the optimal regularization strength, a cross-validation log-likelihood (CVLL) method was proposed by maximizing a CVLL function. Methods: The CVLL function is the likelihood function of the images reconstructed using one subset of a list-mode dataset, based on another subset of the same dataset. This study compares the CVLL method in conventional and total-body PET imaging with contrast-to-noise (CNR) measures. A human subject with lung cancer was injected with ~213 MBq [^{18}F]FDG and scanned for 22 min starting at 60 min with a total-body PET/CT scanner and at 90 min with a conventional PET/CT scanner. An in-house list-mode ordered subset expectation maximization algorithm with a CVLL method module integrated was used for image reconstruction. The same attenuation, random, and deadtime correction methods were used for the two scanners, except for the scatter correction method.

Discussion: The optimal regularization strengths that maximize the CNRs were not perfectly consistent with those determined by the CVLL method. There is potential for both the CVLL and CNR methods to work jointly to select the optimal regularization strength that well balances image resolution and noise.

Conclusion: The CVLL method will facilitate our exploration of the limits of injected activity and scan time, and can be used to guide image reconstruction under different circumstances. We will further validate the CVLL method in total-body and conventional PET imaging of different cancer patients.

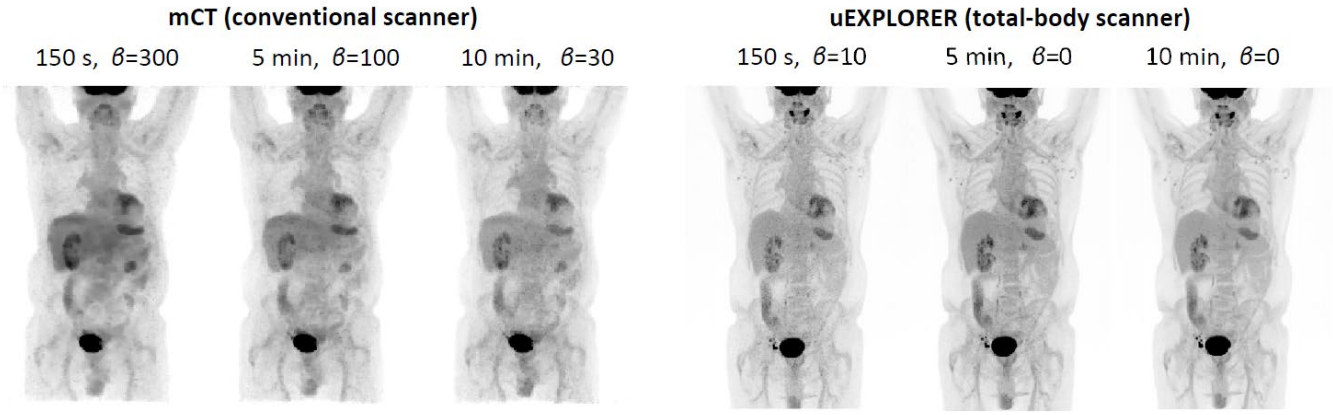

Maximum intensity projections of the in-house reconstructed human (lung cancer patient) images of different scan durations (150 s, 5 min and 10 min), using the optimal regularization strengths β for the mCT and uEXPLORER, respectively.

Kernel SIME: simultaneous estimation of blood input function using a kernel method and its evaluation with total-body PET

[1]Yansong Zhu, [1]Yiran Wang, [1]Quyen Tran, [1,2]Ramsey D. Badawi, [1,2]Simon R. Cherry, [2]Jinyi Qi, [3]Shiva Abbaszadeh, [1]Guobao Wang

[1]Department of Radiology, UC Davis, [2]Department of Biomedical Engineering, UC Davis, [3]Department of Electrical and Computer Engineering, UC Santa Cruz

Introduction: Dynamic PET allows quantification of physiological parameters through kinetic modeling. The accuracy of estimated parameters is influenced by the quality of extracted blood input function. Image-derived (ID) input function (IF) suffers from partial volume effect when it is extracted from small blood vessels such as the case in dynamic brain imaging. Alternatively, optimization-derived input function (OD-IF) from simultaneous estimation (SIME) of input function and kinetic parameters is not stable due to the ill-posedness of the optimization problem. In this work, we developed a new method that exploits ID-IF as a priori information to stabilize SIME through a kernel framework.

Methods: The standard SIME approach estimates an IF and kinetic parameters simultaneously by fitting multiple tissue time activity curves (TACs) of different regions of interest. The approach commonly parameterizes IF using a highly nonlinear model which is difficult to estimate in practice. The proposed kernel SIME method exploits ID-IF as a *priori* information of IF using a kernel representation. The unknown parameters are linear in the model and thus much easier to estimate. The OD-IF by this kernel SIME method was evaluated and compared with ID-IF and OD-IF from conventional SIME using datasets collected from uEXPLORER total-body PET/CT.

Results: The estimated OD-IF by kernel SIME show a good match with the reference input functions. Compared to ID-IF and OD-IF with conventional SIME, estimated kinetic parameters with proposed kernel OD-IF have lower percentage mean absolute error (MAE). Parametric images with proposed kernel OD-IF show similar patterns and close values as those with the reference IF.

Conclusion: We proposed and investigated a kernel SIME method to obtain OD-IF. The method could be potentially applied when major blood pool is not covered in the field of view, such as dynamic brain imaging with a conventional short PET scanner.

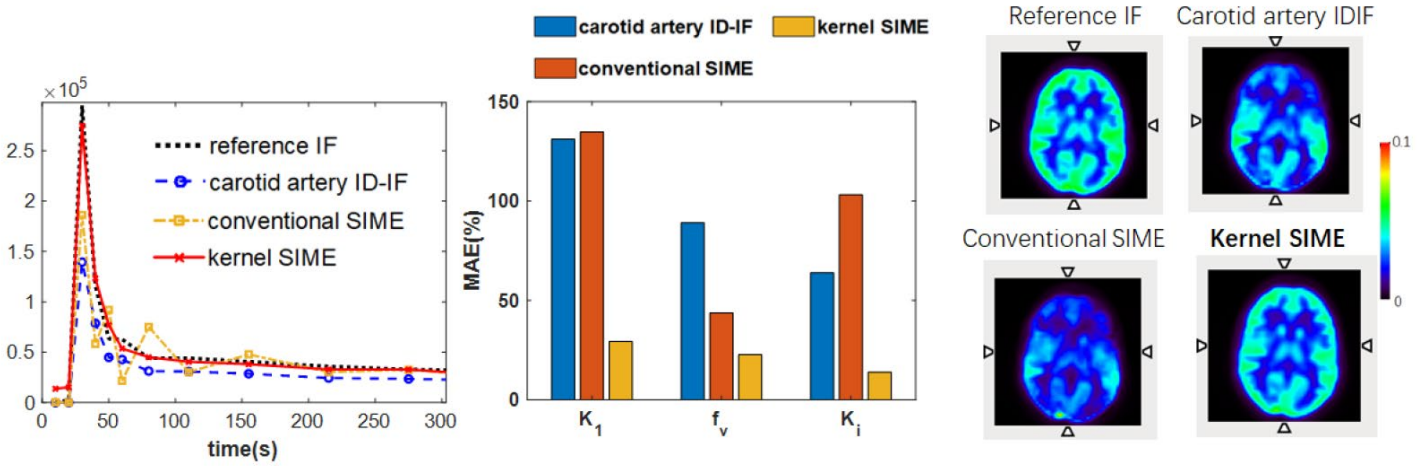

Figure 1. Results for estimated input function (left), mean absolute error for kinetic parameters (middle), and estimated Ki image (right) from different methods.

E-Poster Abstracts

Very low-density lipoprotein triglyceride and free fatty acid clearance rates are linked to brown adipose tissue in women with overweight/obesity	Maria Chondronikola
Serial transthoracic echocardiography for clinical assessment of submassive pulmonary embolism	Roger E. Goldman
A novel method to enhance Positron Emission Tomography detector performance	Xuzhi He
Open Kinetic Modeling Initiatives to Accelerate Quantitative Molecular Imaging Research at UC Davis and in the International Community	Zachary B. Jenner
Financial Analysis of Outpatient Evaluation and Management Billing: A Comparison of IR to Other Specialties.	Cody Key
Diversifying the Subject Cohorts in Total-Body PET Research: A Feasibility Study	Donghoon Kim
Transplant Renal Artery Stenosis Interventions Outcomes at a High-Volume Renal Transplant Center	Patrick Kim
Retrospective review of patients that had percutaneous cholecystostomy tube placement at UCDHS with long-term follow-up	Michael Larson
Utilization of Peripheral Nerve Blocks by Interventional Radiologists for Medicare Beneficiaries from 2010-2018	Andrew Nelson
Total-body PET/CT – first clinical experiences and future perspectives	Quinn Kwan-Tai Ng
A high resolution PET detector for preclinical imaging application	Abdullah Refaey
Personalized Dosimetry for Treatment of Hepatic Cellular Carcinoma using Multiphysics Simulations	Carlos A. Ruvalcaba
Lung airway geometry as an early predictor of autism: A preliminary machine learning-based study	Rebecca Stein-Wexler
Morbidity and Mortality Conferences in Interventional Radiology: Current Patterns and Experiences	Harjot Singh Virk
Trends in Bone Marrow Aspiration & Bone Marrow Biopsy Among Medicare Patients from 2010-2017: Analysis of procedure volume, specialty involvement and cost	Samuel Paran Yap

Very low-density lipoprotein triglyceride and free fatty acid clearance rates are linked to brown adipose tissue in women with overweight/obesity

[1,2]Maria Chondronikola, [2]Jun Yoshino, [2]Raja Ramaswamy, [2]Daniel Giardina, [2]Richard Laforest, [2]Adewole Okunade, [2]Bruce W. Patterson, [2]Bettina Mittendorfer, [2]Richard Wahl, [2]Samuel Klein

[1]Departments of Nutrition and Radiology, UC Davis, [2]Washington University School of Medicine, St. Louis, Missouri

Background and aim: Increased plasma triglyceride (TG) and free fatty acid (FFA) concentrations are likely involved in the pathogenesis of insulin resistance, type 2 diabetes, and coronary heart disease. Studies in rodents demonstrate that BAT is an important site for plasma TG and FFA clearance. However, the interrelationship between BAT, TG, and FFA metabolism in people is not clear.

Materials and Methods: Very low-density lipoprotein (VLDL)-TG and palmitate kinetics were assessed during thermoneutrality by using stable isotopically labeled tracer infusions in women with overweight/obesity who had either a low (LBAT, volume <20 mL) or a high (HBAT, volume ≥20 mL) amount of BAT, assessed by using ^{18}F-fluoro-glucose positron emission tomography after exposure to mild cold. Supraclavicular adipose tissue (SCVAT) biopsies were obtained during thermoneutrality for transcriptomic analysis.

Results: The HBAT group had lower plasma TG concentration and higher VLDL-TG and palmitate clearance rates than the LBAT group. VLDL-TG and palmitate clearance rates were associated with BAT volume and activity independent of age and adiposity. SCVAT expression of genes involved in thermogenesis (i.e., UCP1) and lipid uptake (i.e., LDL-R and GPIHBP1) were higher in the HBAT than the LBAT group.

Conclusion: These data suggest BAT is involved in regulating FFA and VLDL-TG clearance rates and plasma TG concentration in women with overweight/obesity.

Serial transthoracic echocardiography for clinical assessment of submassive pulmonary embolism

[1]Roger E. Goldman, [1]Alvin Lau, [2]Christian Figueredo, [1]Catherine T. Vu

[1]Department of Radiology, UC Davis, [2]Department of Surgery, UC Davis

Background: Limited data currently guide the evaluation and clinical management of patients with submassive pulmonary embolism (PE). Due to the heterogeneity of the submassive PE population, prospective identification of patients who require escalation in treatment is challenging. This investigation evaluates the correlation of serial transthoracic echocardiography (TTE) to clinical outcomes for submassive PE patients.

Methods: A retrospective review was performed to identify patients presenting between 2015 and 2020 to a tertiary care center with acute PE and serial TTE. Inclusion criteria were intermediate-high risk PE according to the European Society of Cardiology guidelines and at least two TTE performed during the hospitalization and prior to administration of thrombolytics or catheter directed therapy (CDT). Exclusion criteria were lack of right ventricular (RV) strain on all serial TTE. 41 patients were identified. The median interval between TTE studies was 95 hours (range 3-287 hours). Individual TTE studies were evaluated for the reported qualitative assessment of RV function. Patients were stratified into cohorts of worsening, unchanged, and improved RV function based on the qualitative TTE assessment. Data regarding the hospital course and clinical outcomes were collected including pressor requirement, intubation requirement, CDT, thrombolytic administration, and 30-day mortality.

Results: 14, 16, and 11 patients, respectively, demonstrated worsening, stable, and improving interval RV function on serial TTE. As compared to the improving RV function cohort, the worsening RV function cohort demonstrated a relative risk of death within 30 days, pressor requirement, intubation requirement and administration of tPA or CDT of 3.93, 1.83, 2.1, and 2.16 respectively. As compared to the improving RV function cohort, the unchanged RV function cohort demonstrated a relative risk of death within 30 days, pressor requirement, intubation requirement, and administration of tPA or CDT of 4.13, 1.83, 1.6, and 0.17, respectively.

Conclusions: Requirements for escalated care and a higher 30-day mortality strongly correlate with lack of improving RV function on serial TTE. Noting the limitations of the small sample size and the retrospective study design, this investigation suggests valuable and actionable clinical information may be acquired through the use of serial TTE in submassive PE patient evaluation and triage.

A novel method to enhance Positron Emission Tomography detector performance

[1]Xuzhi He, [1]Gerard Arino Estrada, [1]Carlotta Trigila, [1,2]Emilie Roncali

[1]Department of Biomedical Engineering, UC Davis, [2]Department of Radiology, UC Davis

Introduction: Positron emission tomography (PET) systems with time-of-flight (TOF) capability have received significant attention in recent years since they improved images signal-to-noise ratio, allowing lower exposure rates for patients. Current commercial systems (e.g., Biograph Vision Quadra PET/CT (Siemens Healthineers)) achieved a 214 ps timing resolution. Timing resolution of less than 30 ps could further improve imaging quality and accelerate imaging reconstruction. Currently, timing resolution is mainly limited by the optical photon (emitted after a gamma interaction in the crystals system) time spread inside the detectors. Here, we propose a statistical method to mitigate their spread by using the interaction position between the gamma and scintillator using optical Monte Carlo simulations in the opensource software GATE.

Methods: The crystal bulk and optical properties (refractive index, stopping power, scintillation yield, decay time) and geometry influence the optical photon spread before detection. Consequently, we separately tested five different materials, four thicknesses (9, 12, 15 and 18 mm), and one cross-section (3 x 3 mm2). We irradiated the material with 511 keV gammas which emitted either scintillation photons (~40 ns) and prompt Cherenkov photons (~10 ps). We grouped them into different bins according to their depth of interaction (DOI). We tested two bin sizes (1 and 3 mm). Cherenkov detection time stamps in each bin were corrected for the DOI time walk and histogrammed to obtain the DOI-corrected detection time distribution, which was characterized by the full width at half of the maximum (FWHM).

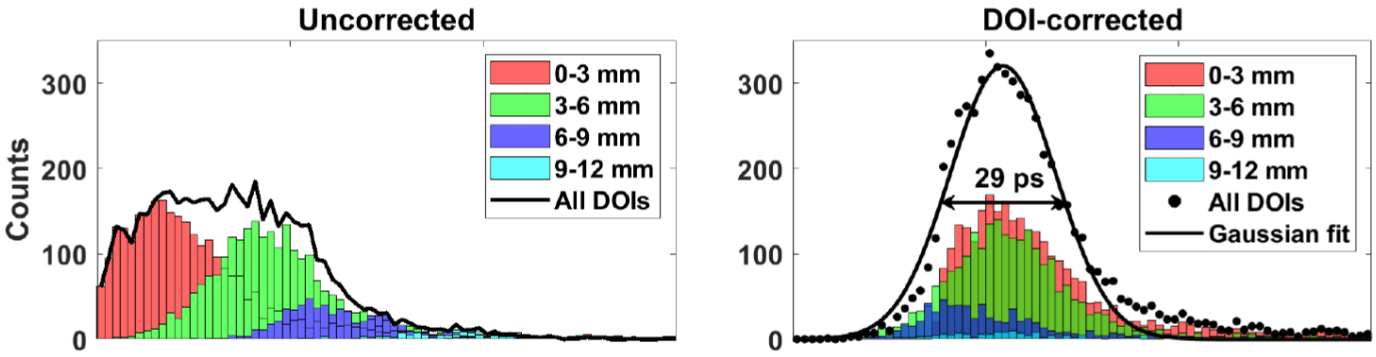

Figure 1: Example of a (left) non corrected and (right) DOI-corrected Cherenkov photons' detection time distribution.

Results: Thanks to the DOI correction, the Cherenkov photons' detection time FWHM was reduced to 26 ps (Figure 1), corresponding to a lower optical time spread. The corrected timing depended on the DOI bin size, scintillator thickness and material properties.

Discussion & Conclusions: DOI corrected Cherenkov photons' timing performance showed promising results and could lead to increased TOF-PET image quality.

Percutaneous antegrade short cholangioscope-aided extracorporeal shock-wave lithotripsy, cholangioplasty, and biliary decompression for acute perforated cholecystitis and septic shock secondary to choledocholithiasis

Zachary B. Jenner, Shan Hansra, Ryan DiGeronimo, Rex Pillai, Amol Shah

Department of Radiology, UC Davis

Clinical history: A 67-year old male presented with two weeks of abdominal pain and developing sepsis (WBC 50k cells/mm3, total bilirubin 6.5 mg/dL, lipase 777 U/L). CT demonstrated choledocholithiasis, severe biliary ductal dilatation, and perforated gallbladder (Figure 1). Clinically, patient was in cholangitis-associated septic shock.

Treatment and results: Endoscopic retrograde cholangiopancreatography was unable to be performed due to unavailable gastroenterologist. Patient was taken urgently to the interventional radiology suite. Percutaneous transhepatic cholangiogram demonstrated perforated gallbladder with small residual gallbladder neck, short dilated cystic duct, and marked biliary ductal dilatation secondary to obstructive choledocholithiasis (Figure 2A). Transhepatic transcholecystic internal/external biliary drain was placed for biliary diversion/decompression. Two weeks later, percutaneous antegrade cholangioscope-aided extracorporeal shock-wave lithotripsy and cholangioplasty was performed (Figure 2B, 2C). Following intervention, cholangiography demonstrated no residual common bile duct stones or obstruction (Figure 2D). Patient has recovered from his acute illness, and is currently awaiting cholecystectomy.

Discussion: Choledocholithiasis treatment varies according to subspecialist skills and availability. Percutaneous intervention is indicated for patients with high risk for complications, altered anatomy, heavy stone burden, and unsuccessful or unavailable endoscopic/surgical treatment. Our case highlights the importance of the interventional radiologist maintaining technical competence with cholangioscopy, lithotripsy, and basket retrieval for cholelithiasis and choledocholithiasis.

Key points: Early biliary decompression in septic shock improves patient morbidity/mortality. Cholangioscope-aided antegrade treatment for choledocholithiasis is a vital skill for interventional radiologists, and is indicated in select patients.

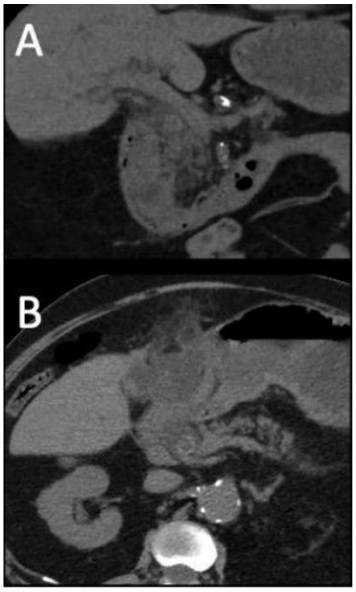

Figure 1.

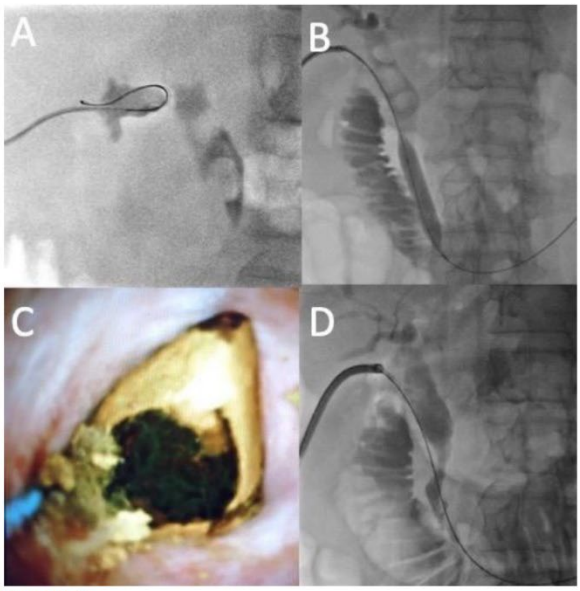

Figure 2.

Financial Analysis of Outpatient Evaluation and Management Billing: A Comparison of IR to Other Specialties

Cody Key

Department of Radiology, UC Davis

Purpose: In the context of clinical interventional radiology (IR) growth and decreasing procedural compensation, understanding trends in reimbursement, submitted charges, and complexity distribution of outpatient evaluation and management (E&M) billing is increasingly important.

Methods: This study utilized data derived from publicly available databases provided by the Center for Medicare and Medicaid Services (CMS). Billing data from the CMS Physicians/Supplier Procedure Summary (PSPS) Master Files from 2010 to 2018 were obtained. Billing codes for new (99201-99205) and established (99211-99205) outpatient encounters were used—stratified into 5 different complexities. Provider codes for diagnostic and interventional radiology were combined and assumed to fall under the description of interventional related work. Similar procedural specialties were analyzed for comparison (vascular, orthopedic, and neurosurgery, interventional pain management, and cardiology).

Results: A Reimbursement for new and established E&M services increased at all complexity levels over the study period, ranging from +4.5 to +10.5%. The overall increase was greater than +10.5% due to a superimposed trend toward billing for more complicated encounters. Compared to similar specialties, IR bills for less complicated E&M services, resulting in the lowest reimbursement for established encounters and second lowest for new encounters.

Submitted charges may be used as a rough proxy for non-Medicare/Medicaid reimbursement. IR submits higher charges than nearly every similar subspecialty at every complexity level. This, with the lower complexity distribution of IR E&M billing, results in near-average charges per 100 Medicare beneficiaries in comparison to similar specialties.

Conclusion: Increasing reimbursement make outpatient E&M services an important source of revenue for all specialties. IR's complexity distribution is lower than other specialties. This could be related to seeing lower complexity patients or to inadequate complexity stratification due to billing and coding. Understanding the cause and implications of variation in submitted charge for outpatient E&M services is an area for future research.

Automated estimation of tissue T1 corrected CBF and ATT from multi-PLD ASL using a 3D CNN

[1,2]Donghoon Kim, [3]Megan Lipford, [4]Hongjian He, [4]Qiuping Ding, [2]Vladimir Ivanovic, [5]Samuel Lockhart, [5]Suzanne Craft, [3]Christopher Whitlow, [1,3]Youngkyoo Jung

[1]Department of Biomedical Engineering, UC Davis, [2]Department of Radiology, UC Davis, [3]Department of Radiology, Wake Forest University, [4]Center for Brain Imaging Science and Technology, College of Biomedical Engineering and Instrumental Science, Zhejiang University, [5]Department of Internal Medicine, Wake Forest University

Introduction: The purpose of this study was to reduce the total scan time of multiple post labeling delay (multi-PLD) pseudo-continuous arterial spin labeling (PCASL) by estimating tissue T1-corrected cerebral blood flow (CBF) and arterial transit time (ATT) maps using a convolutional neural network (CNN).

Methods: Twelve subjects (age: 68.92±6.87 years) had MRI including a multi-PLD PCASL sequence with 6 averages and 9 TIs. To test the feasibility of CNN, ideal ASL tag and control images were generated from the estimated CBF, ATT, and tissue T1 maps using a voxel-wise non-linear model fitting. Nine randomly chosen subjects were used for network training and the remaining 3 were used for testing. Tissue T1 map was estimated from an independent standard CNN. A hierarchically structured CNN (H-CNN) with the PWI and the estimated tissue T1 was used to estimate ATT and CBF because of the physiological relationship between CBF and ATT. Reduced numbers of PLDs were also tested.

Result: Based on the overall root mean square errors (RMSEs) from the non-linear model fitting and H-CNN with the reduced numbers of PLDs, our H-CNN outperformed the non-linear model fitting method in tissue T1-corrected CBF and ATT estimation (Figure 1). Total scan time reductions by the reduced number of PLDs from H-CNN were 11.08%, 9.18%, 29.75%, 31.33%, 50%, 59.18%, and 74.05% by the selected 8, 7, 6, 5, 4, 3, and 2 PLDs, respectively.

Discussion: The proposed method feasibly estimated tissue T1-corrected CBF and ATT from multi-PLD PCASL. The proposed method also showed a higher estimation accuracy than the non-linear model fitting with the reduced numbers of PLDs.

Conclusion: The reported results showed that a smaller number of PLDs can be used to generate tissue T1-corrected CBF and ATT in significantly shorter scan time without significant discrepancy from the reference in multi-PLD PCASL scheme.

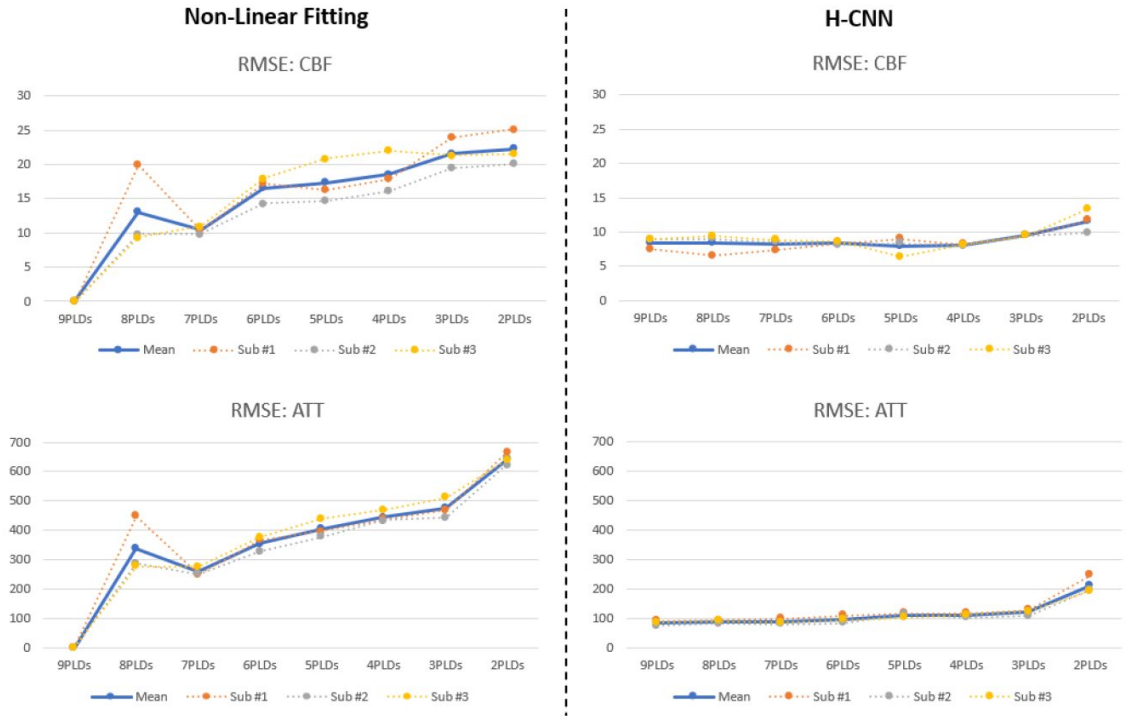

Figure 1. The overall RMSEs of the estimated tissue T1-corrected CBF and ATT maps from the nonlinear fitting (left) and H-CNN (right) using the reduced numbers of PLDs. Tissue T1-corrected CBF and ATT maps from the non-linear model fitting with 9 TIs were used for the ground truth reference images for the RMSE calculations.

Transplant Renal Artery Stenosis Interventions Outcomes at a High-Volume Renal Transplant Center

Patrick Kim

Department of Radiology, UC Davis

Purpose: To provide outcomes analysis of endovascular interventions for transplant renal artery stenosis (TRAS) at a single, high-volume transplant center.

Methods: A single-center retrospective review was performed of all renal visceral angiography and interventions by interventional radiology from August 2010 to July 2020. Out of a total of 245 cases, only cases involving TRAS were further analyzed for primary patency and graft survival. These were then further stratified by type of intervention, whether angioplasty or stenting.

Results: 168 unique patients, 122 male and 46 female, satisfied inclusion criteria. Out of 203 arteriograms for transplant renal artery stenosis, there were 152 interventions performed; 73% angioplasty only, 15% stenting only, and 12% which involved both angioplasty and stenting. Of stented patients, 37% of stents were placed primarily and the remaining 63% were placed as a secondary intervention for refractory stenosis or as a for bail-out strategy.

Overall graft survival was 87% after a mean follow-up of 6.04 years. Of patients who received an intervention, there was 88% graft-survival. Graft failure occurred at a mean of 3.44 years post-intervention. Of the 15 patients who had graft failure, only 1 graft failed due to refractory transplant renal artery stenosis.

Primary patency rate was 86.2% after a mean follow-up of 2.6 years. 3-, 6-, and 12-month rates were 93.9%, 91.6%, and 89.3%, respectively. When further stratified, primary patency rates for primary stents were 87% compared to 84% for angioplasty alone ($p=0.9$) .

Conclusion: At a single-center, the analysis of a decade of endovascular interventions for TRAS shows that angioplasty and/or stenting have reasonable mid-term patency. Angioplasty only strategy has no significant difference in patency rates compared to a stent only strategy. However, for stenting used in combination with angioplasty or as repeat interventions for refractory stenosis and bail-out strategy, the data demonstrates improved patency rates and improved graft survival.

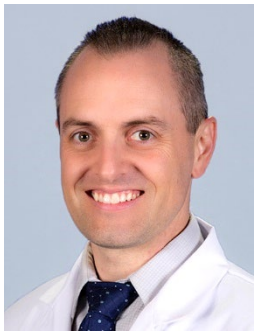

Retrospective review of patients that had percutaneous cholecystostomy tube placement at UCDHS with long-term follow-up

[1] Michael Larson, [2]Katherine Liu

[1]Department of Radiology, [2]UC Davis School of Medicine, UC Davis

INTRODUCTION: Gallbladder infection (cholecystitis) is one of the most common causes for surgical gallbladder removal (cholecystectomy). A growing number of patients are undergoing image-guided percutaneous cholecystostomy tube (PCT) placement before or as an alternative to cholecystectomy. A subset of these patients have the PCT in place for the rest of their life due to being poor surgical candidates. In anticipation of offering minimally-invasive gallbladder thermoablation for such patients that do not want to have a tube for life, we performed a retrospective chart review on patients that underwent PCT at UC Davis.

METHODS: With IRB approval, we performed a retrospective review of patients in the UCDHS radiology picture archiving and communication system up to April 2016 to allow for >5 year follow-up, extracting information from the electronic medical record regarding PCT patients.

RESULTS: We found 122 patients that had PCT placed before May 2016. The mean age was 58.67 years at the time of placement. The M/F ratio was 1.63. Mean BMI was 28.53. Mean American Society of Anesthesiology physical status classification score (ASA) was 2.86. In 21 patients that died with a PCT in place, the median days from placement until death was 36, but the mean was 202.

DISCUSSION: While commonly-taught as a procedure for the elderly and frail, we found that PCT was performed on patients with an average age less than 59 years and average ASA class less than 3. Patients became more obese at the time of PCT placement.

CONCLUSION: This exploratory chart review confirms that there are patients that have PCTs long term that could benefit from gallbladder thermoablation if offered here at UCD.

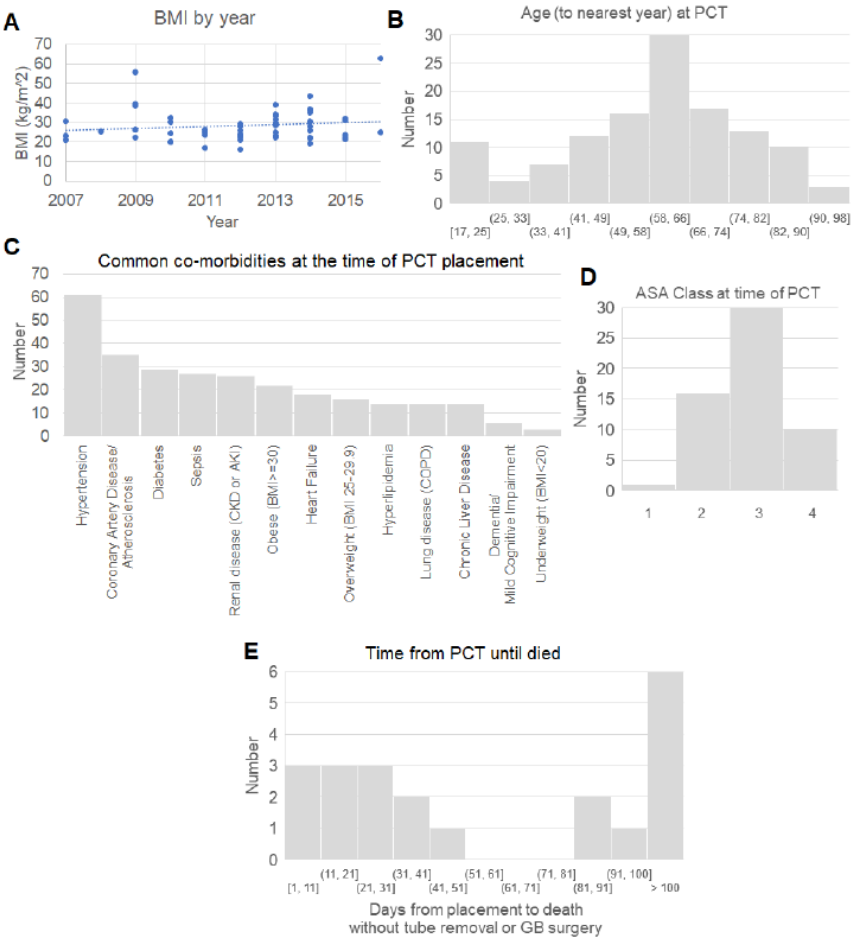

FIGURE: Patient characteristics at the time of PCT placement. A) Patient BMI by year (dotted line represents linear regression), B) histogram of age (to the nearest year), C) common co-morbidities, and D) ASA class at the time of PCT placement. E) Histogram of time from PCT until the patient died in days (n=21).

Utilization of Peripheral Nerve Blocks by Interventional Radiologists for Medicare Beneficiaries from 2010-2018

Andrew Nelson

Department of Radiology, UC Davis

Purpose: Peripheral nerve blocks (PNBs) confer multiple benefits including reduced postprocedural pain and more rapid recovery. While traditionally used for surgical procedures they offer potential benefits for Interventional Radiology patients. Not current data exists regarding the number and type of nerve blocks performed by IR physicians among Medicare patents.

Methods:

This study utilized data derived from publicly available databases provided by the Center for Medicare and Medicaid Services (CMS). Billing data from the CMS Physicians/Supplier Procedure Summary (PSPS) Master Files from 2010 to 2018 were obtained. The following cpt codes were utilized: 64400-64405, 64415-64418, 64420-64421, 64425, 64430, 64445-64450, 64454, 64455, 64624.

Results: The number of peripheral nerve blocks increased among all specialties from 856,230 in 2010 to 1,233,917 in 2018 (+44.1%). In 2018, the majority of peripheral nerve blocks were performed by Anesthesia and Interventional Pain accounting for 54% of the total. Interventional Radiologists performed 4,110 peripheral nerve blocks in 2018 (0.3%) increased from 1,176 in 2010. The five most common nerve blocks performed by IR physicians in 2018 were other (nonspecified), greater occipital, trigeminal, pudendal, and intercostal. The five least common were sciatic, ilio-inguinal, brachial plexus, suprascapular, and axillary nerve blocks. Utilization of peripheral nerve blocks spans a broad range of specialties with family medicine and neurology both performing over 40,000 PNBs in 2018.

Conclusions: Interventional Radiologists are performing an increasing number of peripheral nerve blocks which offer additional pain management options for patients with poor pain tolerance or those that are poor sedation candidates. Future studies will allow for better characterization of the types of blocks being performed by IR physicians as new cpt codes are generated. Dedicated training including rotations with anesthesia/interventional pain service may be beneficial to Interventional Radiology residents.

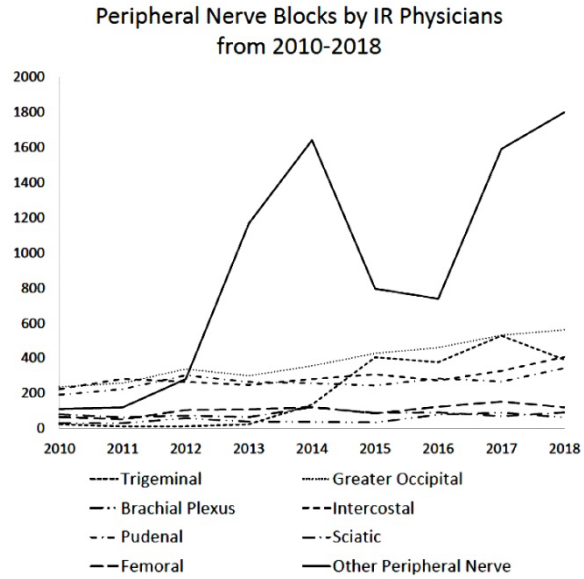

Total-body PET/CT – first clinical experiences and future perspectives

[1]Quinn Kwan-Tai Ng, [1,3]Elizabeth Katherine Anna Triumbari, [2]Negar Omidvari, [1,2]Simon R. Cherry, [1,2]Ramsey D. Badawi, [1]Lorenzo Nardo

[1]Department of Radiology, UC Davis, [2]Department of Biomedical Engineering, UC Davis, [3]Fondazione Policlinico Universitario A. Gemelli IRCCS, Rome, Italy

Total-body PET and long axial field of view (> 77 cm) scanners have been in development since the 90's and now available commercially world-wide. The first total-body PET/CT in the US, uEXPLORER, was installed at UC Davis in 2019 as part of the EXPLORER Consortium. We describe potentials of this scanner, impact on diagnosis and quantification, early clinical challenges, and future perspectives.

The uEXPLORER total-body PET/CT is composed of 8 PET units along the axial direction, forming a total axial length of 194.0 cm and provides signal collection efficiency gain (15–68-fold compared to conventional length PET) and high spatial resolution. This allows for higher sensitivity and improved lesion detection, enhancing clinical applications not readily available on current conventional scanners including: (a) reduction in acquisition times (as low as few minutes) with preservation of diagnostic quality images, beneficial for pediatric/anesthesia patients, motion mitigation, radiotracers with transient uptake; (b) reduction in administered activity with minimal impact on image noise, improving safety and logistical concerns; (c) delayed scanning, increasing detection of small and previously occult lesions by improved clearance of significant background activity and coexisting inflammatory processes; (d) improvement in image quality, allowing for better appreciation of small structures with downstream prognostic consequences; (e) simultaneous total-body dynamic imaging, allowing the measurement of full spatiotemporal distribution of radiotracers, kinetic modeling, and creation of multiparametric images, providing simultaneous whole body physiologic and biologically relevant data.

However, higher sensitivity of total-body scanners bring along new limitations and challenges as this potentially increases false positive findings and delayed scanning can cause logistical workflow issues. Data storage capacity, longer processing/reconstruction time issues are other limitations, but may be overcome by future advancements in reconstruction algorithms and computing hardware. With better understanding of the potential of total-body PET, smooth implementation and optimization of this technology can be achieved.

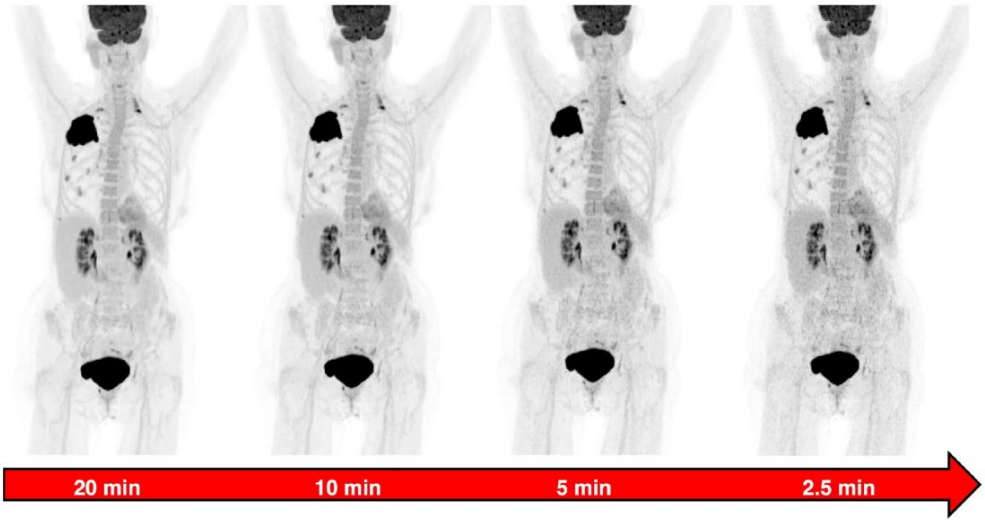

Figure 1: Example of enhanced total-body PET/CT applications. Diagnostic quality images at reduced acquisition times in a patient with right upper lobe lung cancer. Image noise increases at shorter acquisition time; however, the quality of this scan at 2.5 minutes is still within the diagnostic range.

A high resolution PET detector for preclinical imaging application

[1]A. Refeay, [1,2]R. D. Badawi

[1]Department of Radiology, UC Davis,[2]Department of Biomedical Engineering, UC Davis

Abstract

The precision of positron emission tomography (PET) as a quantitative imaging modality in the study of metabolic abnormalities and disease progression in preclinical imaging application depends on specific features in PET detectors such as efficient, accurate, and fast detection capability of gamma rays emitted from the region of interest (ROI) inside the object under investigation. In this study, we are developing a PET detector that matches these features as follows: for high efficiency, high energy resolution, and high light yield, a 10x10 array of LYSO scintillator with crystal dimension 1x1x12 mm^3 is used to absorb and detect the annihilation gammas. For high scintillation photo-detection efficiency (PDE), high gain, and high packing fraction, an 8x8 array of 1x1mm^2 Silicon Photomultipliers (SiPM) are used for detecting the scintillation light. For high compactness, economic-effectiveness, and flexibility, a customized FPGA-based readout electronics is used for signal processing and data acquisition.

The preliminary data showed that an energy resolution of 11.8% at 511 keV photopeak of ^{22}Na is achieved. For crystal identification, all the 100 crystals of LYSO array are resolved and identified. This modular design is being developed to serve in a dedicated high resolution imaging application such as imaging the joints of human finger or small animal preclinical imaging.

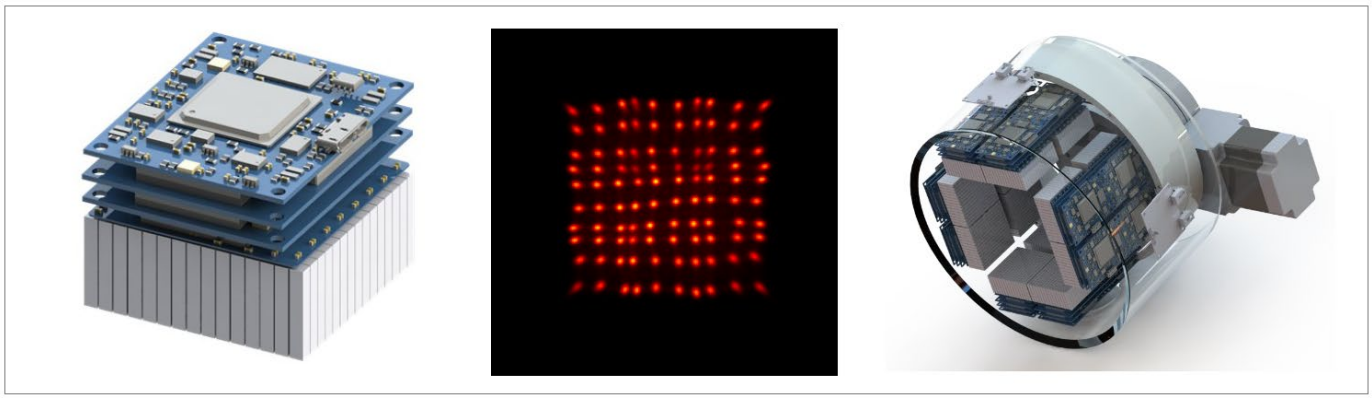

Figure 1. Left: Modular PET detector that is currently being designed. Middle: Flood histogram map or the output image of the scintillation array used in PET detector. Right: CAD design of the Proposed high resolution scanner that can be used for preclinical imaging application.

Personalized Dosimetry for Treatment of Hepatic Cellular Carcinoma using Multiphysics Simulations

[1]Carlos A. Ruvalcaba, [1]Gustavo C. Costa, [1,2]Emilie Roncali

[1]Department of Biomedical Engineering, UC Davis, [2]Department of Radiology, UC Davis

Treating liver cancer patients with transarterial radioembolization uses radioactive yttrium-90 microspheres injected in the hepatic bloodstream via a catheter. Quantification of the absorbed dose in the tumour and normal tissues pre and post treatment is important to optimize the efficacy yet lacks sufficient accuracy and precision. The dose distribution is needed to determine the dose-response and dose-toxicity relationships to mitigate or treat adverse effects. Additionally, radioembolization requires quick clinical decision-making at the time of the yttrium-90 microsphere injection, leading to challenges in implementing accurate and computationally inexpensive pre-treatment models.

We developed CFDose that incorporates clinical patient cone-beam Computed Tomography (CBCT) images and computational fluid dynamics techniques to predict the microsphere transport in the patient liver vasculature. Radiation dosimetry can then be performed from the predicted microsphere transport. Post-treatment Positron Emission Tomography (PET) imaging of the microspheres is used with Monte Carlo simulations to calculate the absorbed dose in individual liver segments.

One of the long-term goals of this work is to compare pre-and post-treatment simulations for treatment planning and evaluation for individual patients. This comparison requires different medical images modalities that often are not all available for a given patient, making it challenging to perform this task.

Preliminary results show similar discrepancies for pre-and post-treatment evaluation for two different patients and activities, when compared to the Medical Internal Radiation Dose (MIRD) formalism, where the absorbed dose for ^{90}Y is defined as $D=49.7\times A_0[MBq]/m[g]$. With CFDose, the calculated absorbed dose is 9.0% lower than that predicted by MIRD while the Monte Carlo absorbed dose is 8.8% lower. Due to patient scan variability, both methods could not be applied to the same patient, but each method shows small underestimations when compared to MIRD. These results build confidence that a close match between pre-and post-treatment evaluation can be ultimately obtained.

CF Dose: A personalized CFD Dosimetry

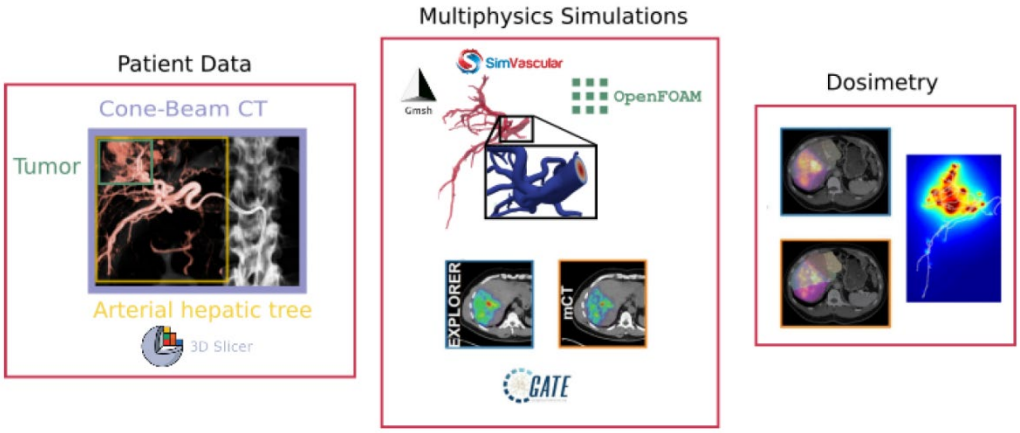

Figure 1:

Overview of the workflow for CFDose, beginning with patient data and ending with personalized dosimetry. In the left most panel, patient cone beam CT data is processed to extract the arterial tree. The center panel gives an overview of the tools used to combine CFD and Monte Carlo simulations. Finally, in the right most panel, the results are combined to give patient specific dosimetry.

Initial MR Compatibility Characterization of a preclinical PET/MRI insert

[1]Aaron Selfridge, [1]Qian Wang, [2]Felipe Godinez, [1,2]Ramsey Badawi

[1]Department of Biomedical Engineering, UC Davis, [2]Department of Radiology, UC Davis

Simultaneous preclinical PET/MRI is well suited to applications which require a dynamic process to be imaged both with PET and MRI. Parametric measurements from PET and functional parameters from MRI can then be used together to gain a better understanding of biological processes. We have designed and built a preclinical PET/MRI insert with sufficiently high sensitivity to image such dynamic processes in mice and rat brains. In this work we assess the impact of the PET insert components on image quality of a preclinical 7T MRI system.

Two opposing PET modules, containing a complete detector stack (Figure 1), were placed in the FOV during an MR acquisition, as they would sit in the completed system. A 3 cm diameter water filled tube was imaged with gradient (GE) and spin echo (SE) sequences in three configurations: No PET components, PET electronics only, and PET detector and electronics. MR images did not present any artifacts indicative of major compatibility issues or changes to magnetic field homogeneity. In the case of the SE sequence, SNR degraded from a factor of 57 at baseline to a factor of 41 in the presence of the PET electronics and detector. Uniformity similarly degrades from 90% to 88%. For the GE sequence the impact on SNR is reversed, increasing from 92 at baseline to 102 when the PET components are used. Uniformity similarly increases from 83 to 85%.

Future work will provide a comprehensive evaluation of both the PET system performance and MRI compatibility of the full detector ring during operation. Additionally, we will evaluate the impact of MRI sequences on PET performance and image quality. These evaluations will help us to make this instrument a core component of our preclinical imaging capabilities.

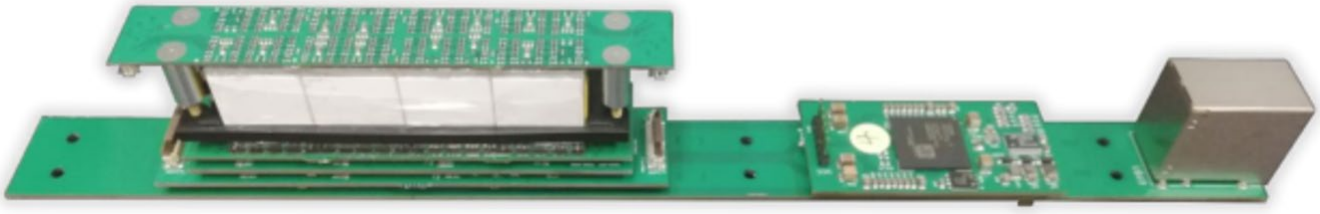

Figure 1. A single PET modules with scintillation crystal, photodetector, and preamplifiers on the left. The FPGA, power components, and connector are on the right. Two opposing modules were used to evaluate MRI compatibility.

Lung airway geometry as an early predictor of autism: A preliminary machine learning-based study

[1]Rebecca Stein-Wexler, [4]Asef Islam, [1]Anthony Ronco, [1]Ellen Cheang, [2]Kyoungmi Kim, [3]Anthony S. Wexler

[1] Department of Radiology, UC Davis, [2]Department of Public Health Science, UC Davis, [3]Departments of Mechanical and Aerospace Engineering; Civil and Environmental Engineering; Land, Air and Water Resources, UC Davis; Davis; Air Quality Research Center, UC, Davis, [4]Department of Computer Science, Stanford University, Stanford, CA

Introduction: This study aimed to determine whether a measurable difference exists in conductive airway geometry between a control population and children with autism spectrum disorder (ASD) using chest computed tomography (CCT) images, with the goal of identifying a biomarker for ASD.

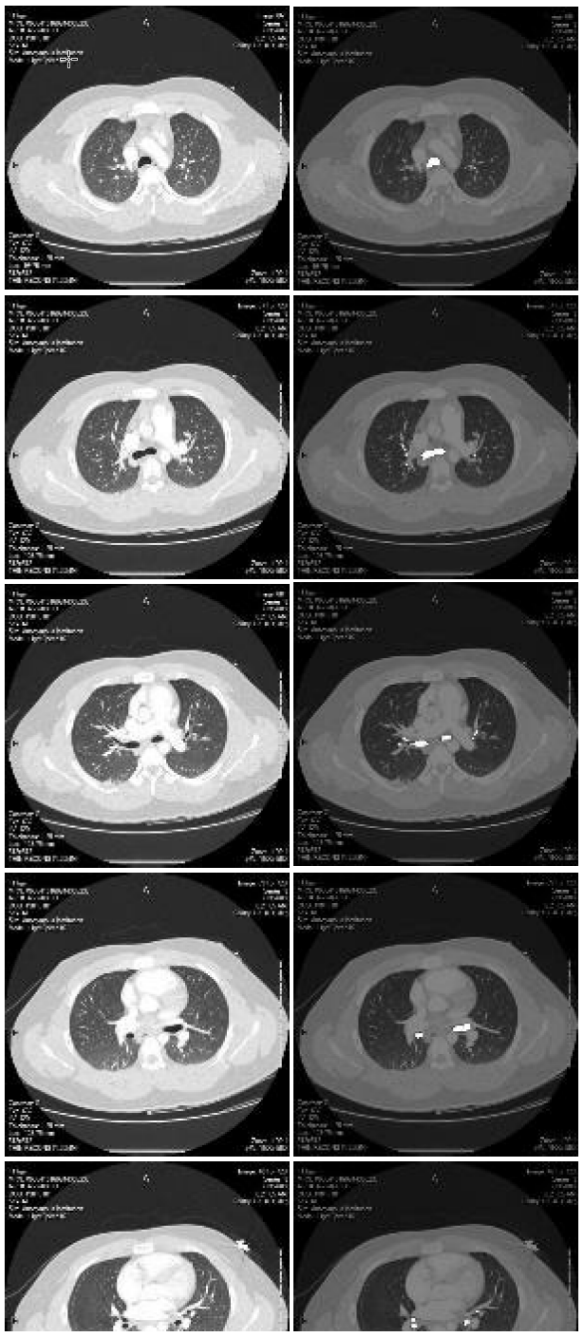

Methods and Materials: 31 CCTs of children with ASD and 23 healthy controls were identified. Principal component analysis (PCA) and support vector machine (SVM) identified significant anatomic parameters. Manual measurements of airway angles from multiplanar reconstructed CCT images were also performed.

Results: The combined PCA and SVM approach achieved an accuracy of nearly 89% using a feature set of 8 airway branching angles. Sensitivity was 94%, but specificity only 78%. The decision rule derived from this approach was tested on manual angle measurements to assess clinical feasibility.

Discussion: Early diagnosis and treatment of ASD is a clinical and public health challenge. Given the pervasiveness of ASD and improved effectiveness of early interventions, biomarkers are needed for early detection. Non-behavioral diagnostic branching of bronchi in generations 3 and 4) were associated with autism, but these anomalies have not been quantified as biomarkers. Our study provides quantitative, statistical analysis of airway geometric parameters predicting autism, derived from CCT. This is the only other study evaluating anatomic airway anomalies in ASD.

Conclusion: There is probably a detectable difference in airway branching angles between children with ASD and healthy controls. However, the significance and clinical applicability of this difference is uncertain. We detected airway anomalies in the same airway generations as prior researchers. Further investigation is needed to evaluate airway anomalies in children with ASD and determine feasibility of this as a biomarker to identify disease.

Figure 1: Typical slices through a CCT. Left: raw scans. Right: CT scans with airways flood-filled with white.

Morbidity and Mortality Conferences in Interventional Radiology: Current Patterns and Experiences

Harjot Singh Virk, R. Torrance Andrews, Ryan DiGeronimo, Roger E. Goldman, Sishir Rao, Eric King, Catherine Tram Vu, Rex Pillai

Department of Radiology, UC Davis

Introduction: The world's first total-body PET scanner, EXPLORER, is operating at UC Davis Health (UCDH). It is utilized for research purposes and routine clinical PET/CT scanning. Given EXPLORER's long axial field-of-view (194 cm) and ultrahigh physical sensitivity, allowing for simultaneous imaging of the entire body, the discovery of incidental findings (IFs) related to clinical problems in research volunteers is likely, potentially requiring follow-up procedures exposing research participants to additional risks.

Methods: A 10-question online survey of practices and experiences with M&M conferencing was administered to members of the Society of Interventional Radiology (SIR).

Results: 604 individual responses were received, with 40% being from university-based practitioners and 60% being from non-university practices. 43% of respondents reported practicing 100% IR, with 28.5% practicing 75-99%, and 11% practicing IR less than 50% of the time. The use of M&M conferencing was significantly greater in university practices (90.7%) than non-university practices (37.1%) and among practitioners performing at least 75% IR (71.2%) than among those practicing less than 75% (28.8%). Conferences were held at least monthly (66.6%), and 56% of events were scored using the SIR severity score. The most common reasons for not using M&M were lack of time and logistical challenges. Among those participating in M&M conferences, the quality assurance (QA) goals of the conference were met at high rates.

Conclusion: Approximately 1/3 of IR practices do not use M&M conferencing, especially those who practice less than 100% IR which tend to favor Radpeer as a QA tool. While Radpeer serves as an effective quality control measure for diagnostic radiology, it is inappropriate for IR procedures which may involve complications, technical errors, or outside factors. Despite the challenges associated with implementation, those who do utilize M&M report multiple benefits and high rates of meeting QA goals.

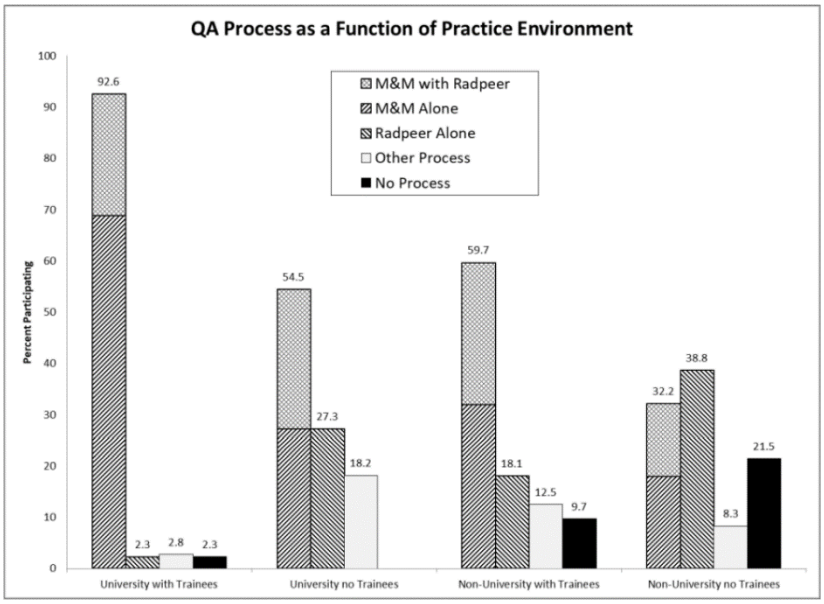

Figure 1. QA process by practice environment; 13 respondents not matched to one of these four practice categories are not included.

Trends in Bone Marrow Aspiration & Bone Marrow Biopsy Among Medicare Patients from 2010-2017: Analysis of procedure volume, specialty involvement and cost

Samuel Paran Yap

Department of Radiology, UC Davis

Purpose: Bone marrow aspiration and bone marrow biopsies can help guide diagnosis and treatment for a variety of disorders. These procedures have traditionally been done by Hematology/Oncology. Among Medicare Patients, minimal data exists on trends in procedure volume and specialty involvement.

Methods: This study utilized data derived from publicly available databases provided by the Center for Medicare and Medicaid Services (CMS). Billing data from the CMS Physicians/Supplier Procedure Summary (PSPS) Master Files from 2010 to 2017 were obtained. The billing codes 38220 and 38221 were used. The Mann-Kendall test was used to analyze for statistically significant trends in procedure volume.

Results: A total of 176,665 bone marrow aspirations and biopsies were billed for in 2010 which decreased significantly ($p<0.01$) to 161,037 (-8.8%) in 2017. The ratio of bone marrow biopsies to aspirations increased from 3.1:1 to 3.8:1 during the study period. By specialty, Hem/Onc accounted for a majority of bone marrow aspirations/biopsies at 64.1% in 2010 followed by Pathology (8.5%) and Advanced Practice Providers (APPs) (8.2%). In 2017 however, Hem/Onc performed 38.9% of total bone marrow aspirations/biopsies with Radiology and APPs increasing their share of these procedures to 22.3% and 20.2% respectively. The specific department/team with which the APPs were associated with is not recorded within the data. Analysis of average submitted charges for bone marrow biopsies revealed that both Hem/Onc and APPs had higher average submitted charges at $483.6 and $512.8 when compared to radiology $367.4 ($p<0.01$).

Conclusion: Among Medicare patients an increasing number of bone marrow aspirations/biopsies are being performed by radiologists at a reduced submitted charge when compared to Hem/Onc and APPs. Exposure and comfort with performing these procedures will be increasingly important for diagnostic and interventional radiologists.

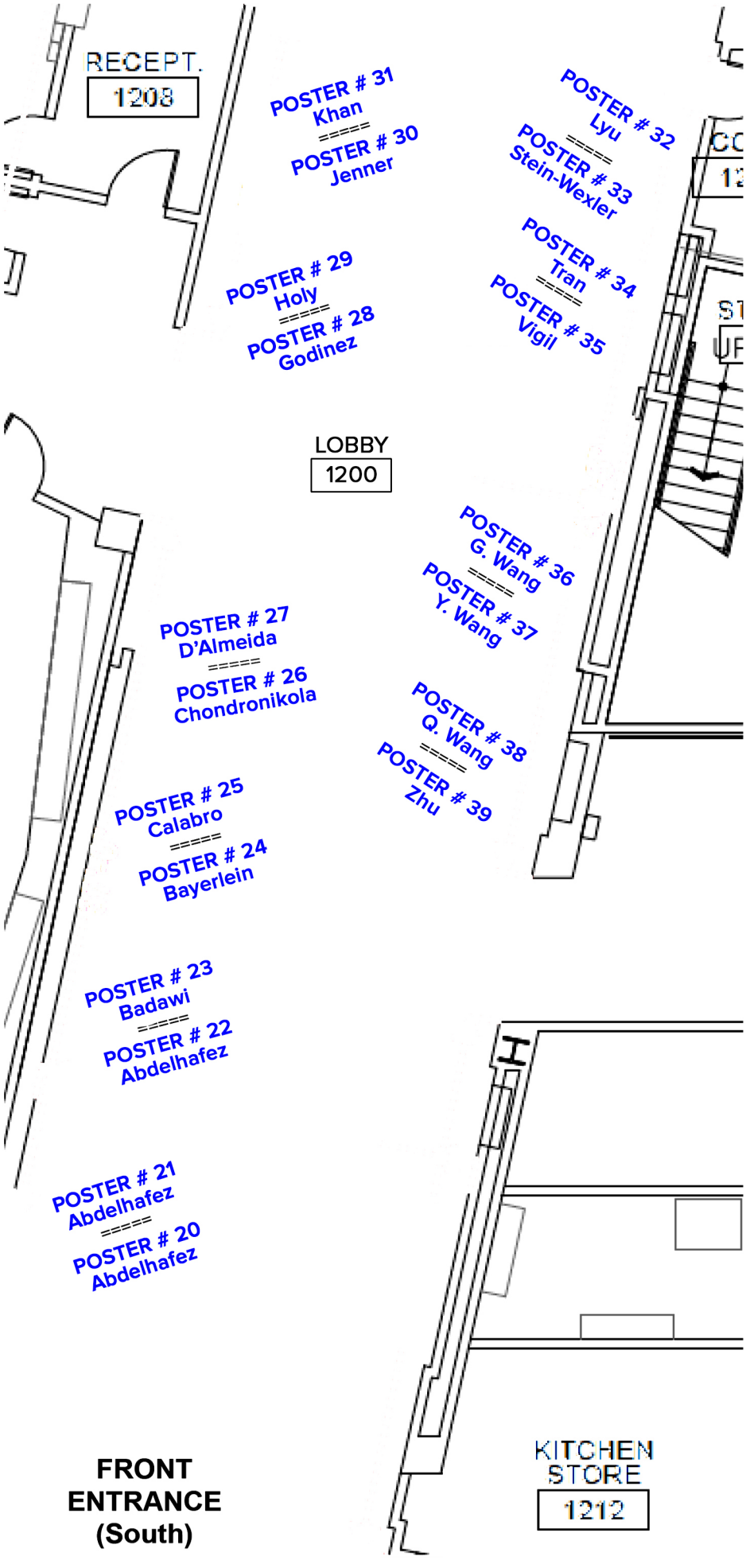
RECEPT.
1208
POSTER # 31
Khan
=====
POSTER # 30
Jenner
POSTER # 32
Lyu
=====
POSTER # 33
Stein-Wexler
POSTER # 29
Holy
=====
POSTER # 28
Godinez
POSTER # 34
Tran
=====
POSTER # 35
Vigil
LOBBY
1200
POSTER # 36
G. Wang
=====
POSTER # 37
Y. Wang
POSTER # 27
D'Almeida
=====
POSTER # 26
Chondronikola
POSTER # 38
Q. Wang
=====
POSTER # 39
Zhu
POSTER # 25
Calabro
=====
POSTER # 24
Bayerlein
POSTER # 23
Badawi
=====
POSTER # 22
Abdelhafez
POSTER # 21
Abdelhafez
=====
POSTER # 20
Abdelhafez
KITCHEN
STORE
1212
FRONT
ENTRANCE
(South)